JCI insight

RESEARCH ARTICLE

An SFTPC BRICHOS mutant links epithelial ER stress and spontaneous lung fibrosis

Jeremy Katzen,[1] Brandie D. Wagner,[2] Alessandro Venosa,[1] Meghan Kopp,[1] Yaniv Tomer,[1] Scott J. Russo,[1] Alvis C. Headen,[1] Maria C. Basil,[1] James M. Stark,[3] Surafel Mulugeta,[1] Robin R. Deterding,[4] and Michael F. Beers[1,5]

[1]Pulmonary, Allergy, and Critical Care Division, Department of Medicine, Perelman School of Medicine, University of Pennsylvania, Philadelphia, Pennsylvania, USA. [2]Department of Biostatistics and Informatics, Colorado School of Public Health, Aurora, Colorado, USA. [3]Division of Pediatric Pulmonology, Department of Pediatrics, University of Texas Health Science Center, Houston, Texas, USA. [4]Department of Pediatrics and Breathing Institute, University of Colorado School of Medicine, Aurora, Colorado, USA. [5]Penn Center For Pulmonary Biology, University of Pennsylvania, Perelman School of Medicine, Philadelphia, Pennsylvania, USA.

Alveolar type 2 (AT2) cell endoplasmic reticulum (ER) stress is a prominent feature in adult and pediatric interstitial lung disease (ILD and ChILD), but in vivo models linking AT2 cell ER stress to ILD have been elusive. Based on a clinical ChILD case, we identified a critical cysteine residue in the surfactant protein C gene (*SFTPC*) BRICHOS domain whose mutation induced ER stress in vitro. To model this in vivo, we generated a knockin mouse model expressing a cysteine-to-glycine substitution at codon 121 (C121G) in the *Sftpc* gene. *Sftpc*^{C121G} expression during fetal development resulted in a toxic gain-of-function causing fatal postnatal respiratory failure from disrupted lung morphogenesis. Induced *Sftpc*^{C121G} expression in adult mice resulted in an ER-retained pro-protein causing AT2 cell ER stress. *Sftpc*^{C121G} AT2 cells were a source of cytokines expressed in concert with development of polycellular alveolitis. These cytokines were subsequently found in a high-dimensional proteomic screen of bronchoalveolar lavage fluid from ChILD patients with the same class of *SFTPC* mutations. Following alveolitis resolution, *Sftpc*^{C121G} mice developed spontaneous pulmonary fibrosis and restrictive lung impairment. This model provides proof of concept linking AT2 cell ER stress to fibrotic lung disease coupled with translationally relevant biomarkers.

Introduction

Adult interstitial lung disease (ILD) and pediatric childhood ILD (ChILD) are defined pathologically by interstitial fibrosis, inflammation, or a combination of fibrosis and inflammation (1, 2). With thickening of the alveolar interstitium causing impairment in effective gas exchange, the clinical course is often progression to chronic respiratory failure (3, 4). Over the past decade, the alveolar type 2 (AT2) cell has come to the forefront as a key driver of lung fibrosis and ILD (5, 6). Focus on the AT2 cell is in part due to the identification of disease-causing mutations in the AT2 cell–restricted surfactant protein C gene (*SFTPC*) in both pediatric patients with ChILD and in a subset of adult patients with familial ILD (7–9). The recent demonstration by our group of the occurrence of spontaneous lung fibrosis with expression of the *Sftpc*^{I73T} trafficking mutation in a preclinical mouse model has provided further proof of concept for the AT2 cell as a proximal driver of ILD (10). While the *SFTPC*^{I73T} mutation, which causes a block in AT2 cell macroautophagy, is the most common clinical *SFTPC* mutation identified, a majority of the 60 described mutations in the *SFTPC* gene associated with human disease occur in the distal C-terminal (residues 94–197) BRICHOS domain of the surfactant protein C (SP-C) pro-protein (proSP-C). Their expression results in pro-protein aggregation and induction of ER stress (11–16). These cases further highlight the proximal position of the AT2 cell in the pathogenesis of pulmonary fibrosis and suggest that AT2 cell ER stress may provide a broader mechanistic link between *SFTPC* BRICHOS mutation–associated pediatric ChILD and adult ILD.

Markers of ER stress are also a prominent feature in lung epithelium from patients with sporadic idiopathic pulmonary fibrosis (IPF), the most common adult ILD (17); however, the role of epithelial ER

Conflict of interest: RRD is on the Boehringer Ingelheim Pediatric Interstitial Lung Disease Advisory Board.

Submitted: November 12, 2018
Accepted: January 31, 2019
Published: March 21, 2019

Reference information:
JCI Insight. 2019;4(6):e126125.
https://doi.org/10.1172/jci.insight.126125.

stress in disease pathogenesis is unclear. In vivo proof-of-concept studies linking *SFTPC* BRICHOS mutations, ER stress, and pulmonary fibrosis have been plagued by over- and underexpression of the mutant pro-protein isoforms, and have failed to establish a mechanistic connection. While constitutive transgenic expression of a highly aggregation prone *SFTPC* mutation (*SFTPC*$^{\Delta exon4}$) resulted in disrupted lung morphogenesis with prenatal lethality (18), inducible expression of a less-severe mutation (*SFTPC*^{L188Q}) at lower levels produced increased susceptibility to bleomycin fibrosis, but not spontaneous fibrotic remodeling (19). This finding suggested that epithelial ER stress may not be a driver of fibrosis per se, but a marker of a dysfunctional and vulnerable epithelium requiring a "second hit" to cause disease.

Given the low level of *SFTPC* expression induced in *SFTPC*^{L188Q} mice, we sought to challenge this notion with the hypothesis that a more-severe *SFTPC* BRICHOS mutation expressed at a more biologically relevant level would produce ER stress–based toxic gain of function resulting in a dysfunctional epithelial cell capable of driving a spontaneous lung phenotype. Based upon a pediatric case of ChILD with a mutation in the cysteine at codon 121 (C121), and previous ultrastructural analysis demonstrating that the disulfide bond formed between C121 and cysteine 189 of the BRICHOS domain mediates the primary folding of the proSP-C primary translation product (20), we generated a murine model (*Sftpc*^{C121G}). Consistent with a misfolded isoform, the *Sftpc*^{C121G} pro-protein is proximally retained in the ER and induces substantial epithelial ER stress both in vitro and in vivo. The resultant lung phenotype of AT2 cell–driven spontaneous inflammation and subsequent fibrotic remodeling provides proof of concept linking *SFTPC* BRICHOS mutations and pulmonary fibrosis. The translational relevance of this model was further corroborated by a high-dimensional proteomic analysis of bronchoalveolar lavage fluid (BALF) from pediatric patients with *SFTPC* BRICHOS mutation–associated ChILD showing overlapping cytokine expression. The *Sftpc*^{C121G} model, with relevant biomarker elaboration, thus establishes that AT2 cell ER stress is a sufficient driver for spontaneous lung inflammation and aberrant fibrotic lung remodeling.

Results

In vitro expression of a clinical SFTPC cysteine 121 mutation induces ER stress by a proximally retained SP-C pro-protein. A male child of an uncomplicated pregnancy was born at 38 weeks gestation by spontaneous vaginal delivery to a 27-year-old mother. He subsequently developed respiratory failure in the first day of life, requiring endotracheal intubation and mechanical ventilation. He received exogenous surfactant, and was extubated and transitioned to nasal cannula supplemental oxygen. At 2 months of age, a second episode of respiratory failure occurred, requiring tracheostomy for chronic mechanical ventilation. Chest imaging at 3 months demonstrated diffuse ground glass opacities (Figure 1A). Subsequently, a clinical pathologic analysis of an open lung biopsy (Figure 1B) showed ChILD histology with enlargement of airspaces, interstitial widening, inflammatory infiltrate, and prominent AT2 cell hyperplasia. Bronchoalveolar lavage demonstrated increased cellularity (755 cells/ml) with elevated neutrophils (20%). The patient was ultimately weaned from the ventilator and decannulated 2 years later. Genetic testing demonstrated a heterozygous *SFTPC* mutation in the BRICHOS domain, c.362 G>A (p.C121Y), without *SFTPB* or ATP binding cassette A3 (*ABCA3*) mutations.

In vitro modeling was performed to define the functional consequences of C121 mutations on proSP-C biosynthesis. Plasmids containing EGFP-tagged WT *SFTPC* (EGFP/SP-C^{WT}) and 2 *SFTPC* mutants, EGFP/SP-C^{C121Y} and EGFP/SP-C^{C121G}, were transfected into HEK293 cell lines, which were interrogated for cellular expression patterns and posttranslational processing. The *SFTPC*^{C121G} mutation, which has also been described clinically (21), was selected in addition to the clinical *SFTPC*^{C121Y} mutation to generalize the importance of disulfide bonding in the pro-protein via the C121 thiol (20). In contrast to the WT isoforms, Western blot analysis of cell lysates showed a primary proSP-C translation product containing either cysteine mutant failed to undergo normal processing to a cleaved intermediate pro-protein (Figure 1C). Subsequent cotransfection of HEK293 cells with EGFP/SP-C^{WT} or EGFP/SP-C^{C121G} and DsRed-tagged *ABCA3* (DsRed/ABCA3) to mark lysosome-related organelles (LROs) demonstrated colocalization between EGFP/SP-C^{WT} and DsRed/ABCA3, but reticular patterning without colocalization of the EGFP/SP-C^{C121G} isoform in LROs (Figure 1D). Expression of the proximally retained mutant pro-proteins induced an ER stress response in vitro, as transfected HEK293 cell lysates demonstrated increases in BiP (GRP78) protein in cells expressing either *SFTPC* mutation compared with WT *SFTPC* (Figure 1E). This was consistent with previously published in vitro studies of *SFTPC* BRICHOS mutants, which have demonstrated BiP to be a reliable marker of the ER stress response (13, 15). These data collectively define a critical role of the C121 residue in the biosynthetic routing and processing of proSP-C, and reveal an ER stress toxic gain of function with *SFTPC*^{C121} mutations.

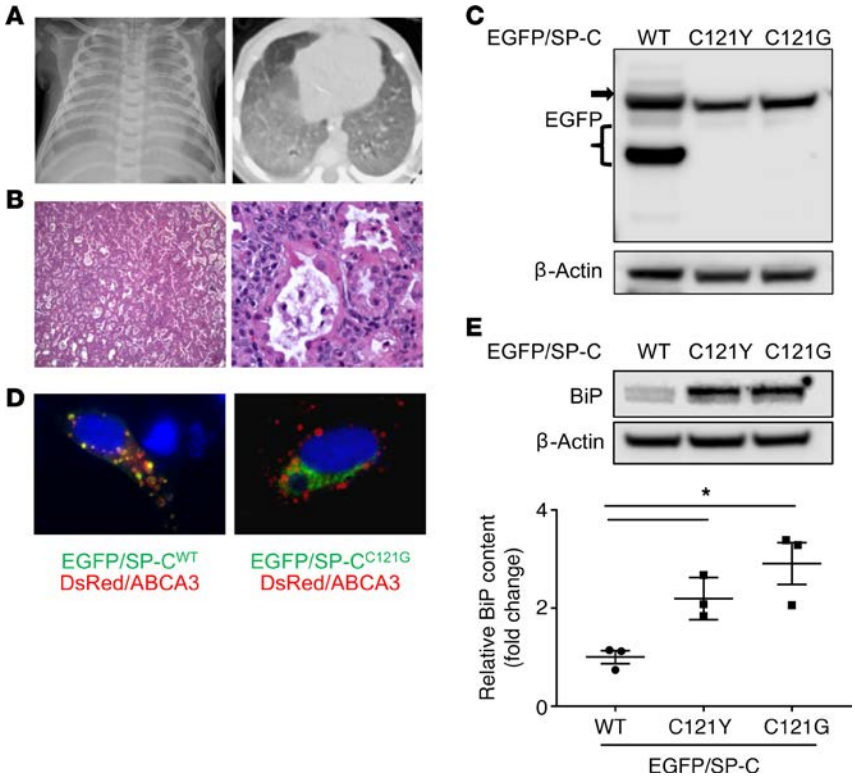

Figure 1. In vitro modeling of a clinical *SFTPC*^{C121Y} mutation identifies mistrafficked pro-protein and epithelial ER stress with mutagenesis of codon 121 in *SFTPC*. (**A**) Chest imaging of a 3-month-old patient with heterozygous *SFTPC*^{C121Y} mutation shows bilateral diffuse hazy opacity on chest radiograph (left) and diffuse ground glass opacities on chest CT (right). (**B**) H&E staining of patient lung biopsy demonstrates diffuse abnormality in lobular architecture, with mild enlargement of airspaces and mild to moderate interstitial widening, airspaces filled by foamy macrophages, scattered neutrophils, and eosinophilic material suggestive of proteinosis (original magnification, ×4 left and ×20 right). (**C**) HEK293 cells were transiently transfected with either EGFP/SP-C^{WT} or EGFP/SP-C^{C121} mutants as indicated, and cell lysates harvested at 48 hours were subjected to Western blotting for EGFP. An SP-C primary translation product (black arrow) was detected in all transfections; however, no processing intermediates (black bracket) were observed with either EGFP/SP-C^{C121} mutation. Representative of 3 independent experiments. (**D**) HEK293 cells transiently cotransfected with either EGFP/SP-C^{WT} or EGFP/SP-C^{C121G} and DsRed/ABCA3 and subjected to immunfluorescence microscopy, demonstrating colocalization of EGFP/SP-C^{WT} with DsRed/ABCA3, but a reticular expression pattern of EGFP/SP-C^{C121G} without DsRed/ABCA3 colocalization (original magnification, ×60). (**E**) Cell lysates of HEK293 cells 48 hours after transfection with either EGFP/SP-C^{WT} or EGFP/SP-C^{C121} mutants as indicated were subjected to Western analysis for BiP (top). Representative Western blot of n = 3. Quantitative densitometry (bottom) normalized to β-actin showing increases in BiP with the cysteine mutants compared to EGFP/SP-C^{WT}. n = 3. *P < 0.05 vs. EGFP/SP-C^{WT} by 1-way ANOVA with Dunnett's multiple comparison test.

Constitutive expression of the Sftpc^{C121G} mutation in vivo phenocopies the human pediatric mutation. Given the importance of C121 in the processing of proSP-C in vitro, we utilized an embryonic stem (ES) cell recombineering strategy to selectively knock in a homologous cysteine-to-glycine substitution at codon 121 (C121G) to the endogenous mouse *Sftpc* locus. Given that the functional consequences of each cysteine mutant isoform were equivalent in vitro, the C121G missense substitution was chosen for the in vivo knockin model to limit confounding variables related to residue side chain size, hydrophobicity, or potential posttranslational modification of a tyrosine residue. The resultant founder line (*Sftpc*$^{C121Gneo/C121Gneo}$) retained a PGK-neomycin (PGK-neo) cassette in intron 4 flanked by locus of X-over P1 (loxP) sites (Supplemental Figure 1A; supplemental material available online with this article; https://doi.org/10.1172/jci.insight.126125DS1). Retention of the PGK-neo cassette rendered the *Sftpc*^{C121Gneo} gene hypomorphic, a strategy employed for knockin models of toxic gain-of-function mutations (10, 22, 23), with mRNA levels in homozygous *Sftpc*^{C121Gneo} animals limited to ~6% that of littermates expressing 2 *Sftpc*^{WT} alleles (Supplemental Figure 1B). Despite AT2 cells lacking expression of proSP-C (Supplemental Figure 1C) and consistent with the phenotype of the *Sftpc*-knockout mouse (24), the founder line was devoid of a spontaneous inflammatory or fibrotic phenotype when aged up to 52 weeks (Supplemental Figure 1, D–F).

To evaluate the effect of increasing *Sftpc*^{C121G} expression in the developing lung, we constitutively removed the loxP-flanked PGK-neo cassette from *Sftpc*^{C121Gneo} alleles by crossing the *Sftpc*$^{C121Gneo/C121Gneo}$ founder line to mice heterozygous for the CMV-Cre recombinase (a "deleter" line) (25). The resultant progeny were either *Sftpc*$^{WT/C121Gneo}$ in mice not receiving the CMV-Cre allele or heterozygous for the activated *Sftpc*^{C121G} allele (*Sftpc*$^{WT/C121G}$) in mice receiving the CMV-Cre allele (Figure 2A). Consistent with a dominant negative effect, heterozygous expression of *Sftpc*^{C121G} caused abnormal processing of the WT SP-C pro-protein, with reduced processing intermediates on Western blotting for proSP-C (Figure 2B) and an 84.7% ± 3.2% (mean ± SD, n = 4) reduction in mature SP-C (mSP-C) protein in P2.5 lung homogenates (Figure 2C). This finding recapitulates data from *SFTPC* BRICHOS mutation patients whereby heterozygous expression of the *SFTPC* mutation dramatically blocks pro-protein processing, reducing the amount of mSP-C in patients' BALF (26–28). Previous in vitro studies have shown mechanistically that heteromeric association between mutant and WT proSP-C proteins is responsible for disruption of the intracellular trafficking of the WT proSP-C isoform (16, 29, 30).

The constitutive *Sftpc*^{C121G} expression model phenocopied many of the features of the pediatric disease (27, 31). Similar to some cases of ChILD, including the one presented here (Figure 1), a toxic gain of function was observed, with *Sftpc*$^{WT/C121G}$ mice developing lethal postnatal respiratory failure with a median survival of 2.5 days (Figure 2D). *Sftpc*^{C121G} expression manifested as respiratory distress and cyanosis between P1.5 and P3.5 (Figure 2E), with lung histology of distorted architecture, enlargement of airspaces, interstitial widening, inflammatory infiltrate, and proteinacious fluid in the airspaces (Figure 2F) — features resembling the histology in the clinical *SFTPC*^{C121Y} case (Figure 1B).

Expression of mutant Sftpc^{C121G} *in adult mice results in ER-retained SP-C pro-protein and ER stress*. To evaluate the cellular effect of *Sftpc*^{C121G} expression in the adult mouse, the *Sftpc*^{C121Gneo} founder line was crossed to the Rosa26-ERT2-Cre line (*R26*^{Cre}) to generate a line (*Sftpc*^{C121G} *R26*^{Cre}) capable of tamoxifen-mediated Cre recombinase removal of the inhibitory PGK-neo cassette from *Sftpc*^{C121Gneo} alleles (Figure 3A). In the absence of tamoxifen, adult homozygous *Sftpc*$^{C121G/C121G}$ *R26*^{Cre} animals injected with vehicle (i.p. oil) retained a phenotype identical to that of the *Sftpc*$^{C121Gneo/C121Gneo}$ founder line without substantial leakiness of the *R26*^{Cre} locus, as shown by the absence of detectable proSP-C on immunohistochemistry (Supplemental Figure 2). Given the absence of a lung phenotype in *Sftpc*$^{C121G/C121G}$ *R26*^{Cre} mice with i.p. oil and the extreme hypomorphic *Sftpc* expression in the founder line, we selected tamoxifen-injected *Sftpc*^{WT} *R26*^{Cre} mice as controls, given previously described cre lung toxicity (32). At 7 days after administration of tamoxifen (500 mg/kg), *Sftpc*^{C121G} mRNA increased to 26.2% ± 4.9% (mean ± SD, n = 7) versus *Sftpc*^{WT} controls (Figure 3B), a 4-fold increase from the hypomorphic *Sftpc*$^{C121Gneo/C121Gneo}$ founder line. Using quantitative real-time PCR (qRT-PCR) to estimate PGK-neo cassette numbers, the efficiency of loxP-mediated recombination in purified AT2 cells isolated 1 week after tamoxifen treatment was 92.4% ± 3.1% (mean ± SD, n = 4) referenced against *Sftpc*$^{C121Gneo/C121Gneo}$ mice. Despite a substantial increase in *Sftpc*^{C121G} mRNA, Western blot analysis of the phospholipid-enriched large aggregate surfactant fraction of BALF from tamoxifen-treated *Sftpc*$^{C121G/C121G}$ *R26*^{Cre} mice showed no evidence of extracellular mSP-C protein (Figure 3C). The absence of the mSP-C protein was the result of a failure to process translated proSP-C, as AT2 cell lysates from these mice showed a single 21-kDa pro-protein band, corresponding to the unprocessed primary translational product. In contrast, 23- and 21-kDa pro-protein bands (23 kDa corresponding to the palmitoylated post-ER pro-protein) with processing intermediates from 8 to 15 kDa were observed in *Sftpc*^{WT} *R26*^{Cre} controls (Figure 3D) (33, 34). Furthermore, lung sections of tamoxifen-treated *Sftpc*$^{C121G/C121G}$ *R26*^{Cre} mice demonstrated a reticular pattern of the mutant proSP-C with significant colocalization with the ER marker KDEL, signifying substantial ER retention (Figure 3E). Thus, interrogation of the adult *Sftpc*$^{C121G/C121G}$ *R26*^{Cre} mice revealed ER retention of the mutant proSP-C in vivo without evidence for posttranslational palmitoylation from post-Golgi or proteolytic processing, consistent with the in vitro data (Figure 1) and what has been reported in *SFTPC* BRICHOS patients (27, 35).

ER retention of mutant proSP-C C121G induced activation of the unfolded protein response (UPR) in the pulmonary epithelium, as reflected by a substantial increase in *BiP* mRNA in AT2 cells isolated from mouse lungs as early as 7 days after tamoxifen treatment (Figure 4A). In a corresponding fashion, BiP protein was also detected in AT2 cells by both immunohistochemical staining of cells localized to corners of alveoli (Figure 4B) and Western blotting of AT2 cell lysates (Figure 4C). Consistent with our prior in vitro modeling (36), the *Sftpc*^{C121G} AT2 cell phenotype was distinct from the *Sftpc*^{I73T} model, where expression of that mutant isoform caused a block in macroautophagy and failed to generate substantial AT2 cell BiP expression (Supplemental Figure 3)(10).

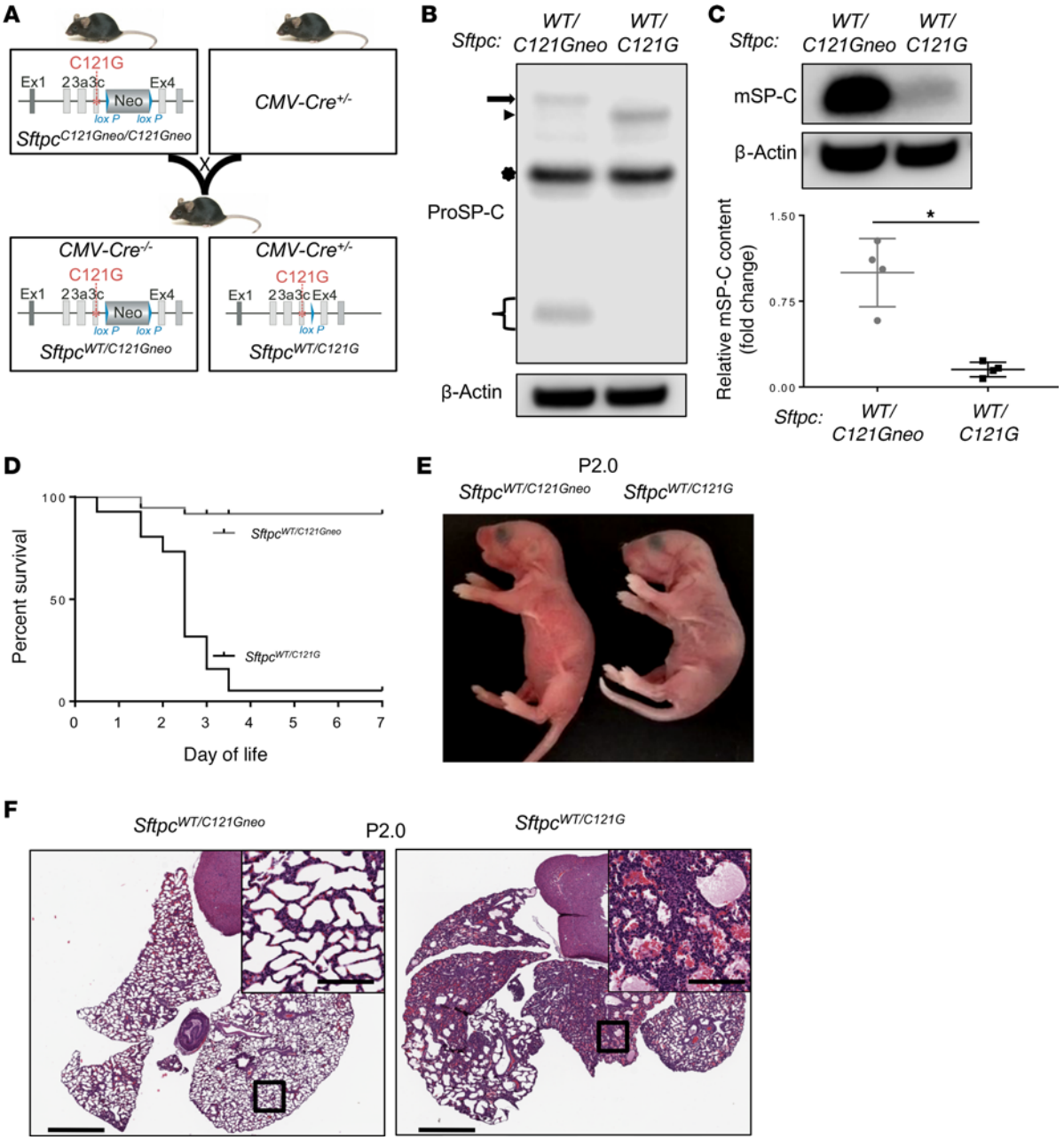

Figure 2. Constitutive expression of the *Sftpc*^{C121G} mutation in vivo causes a lethal toxic gain of function. (**A**) Schematic for generation of mice constitutively expressing *Sftpc*^{C121G} alleles. Breeding of the *Sftpc*$^{C121Gneo/C121Gneo}$ line to *CMV-Cre* mice yields litters with heterozygous constitutive expression of the *Sftpc*^{C121G} mutation (*Sftpc*$^{WT/C121G}$). (**B**) Western blotting of lung homogenates from day P2.5 for proSP-C expression shows aberrant banding pattern, with heterozygous *Sftpc*^{C121G} expression with decreased processing intermediates (arrow, *Sftpc*$^{WT/C121Gneo}$ proSP-C highest-molecular-weight translational product; arrowhead, *Sftpc*$^{WT/C121G}$ highest-molecular-weight translational product; star, nonspecific bands; brackets, processing intermediates). (**C**) Top: Representative Western blot of lung homogenates from P2.5 for mature SP-C (mSP-C). Bottom: Dot plots of mean and SEM of mSP-C densitometry expressed as fold change to *Sftpc*$^{WT/C121Gneo}$. *$P < 0.05$ using unpaired 2-tailed *t* test with normalization to β-actin loading control. (**D**) Kaplan-Meir survival analysis showing high lethality with constitutive *Sftpc*^{C121G}expression ($n = 41$ and 37 for *Sftpc*$^{WT/C121G}$ and *Sftpc*$^{WT/C121Gneo}$, respectively). $P < 0.001$ by log-rank (Mantel-Cox) test. (**E**) Representative photographs of P.2.0 pups show development of cyanosis in the *Sftpc*$^{WT/C121G}$ animal. (**F**) Representative lung histology (×4 magnification) of P2.0 *Sftpc*$^{WT/C121G}$ pups with heterogeneous areas (×10 magnification inset) of thickened septae with proteinaceous fluid in the alveolar space. Scale bars: 500 μm, 200 μm (insets).

The UPR utilizes 3 signaling pathways: IRE1/XBP1, PERK/ATF4, and ATF6. Each pathway was interrogated in the AT2 cells from *Sftpc*$^{C121G/C121G}$ *R26*^{Cre} and control mice after tamoxifen treatment. The IRE1 pathway was activated, as demonstrated by an increase in the ratio of active spliced *Xbp1(S)* to unspliced *Xbp1(U)* mRNA (Figure 4D), and downstream activation of JNK signaling, as shown by increased phosphorylated JNK (Figure 4E). The PERK/ATF4 pathway was found to be activated by an increase in both

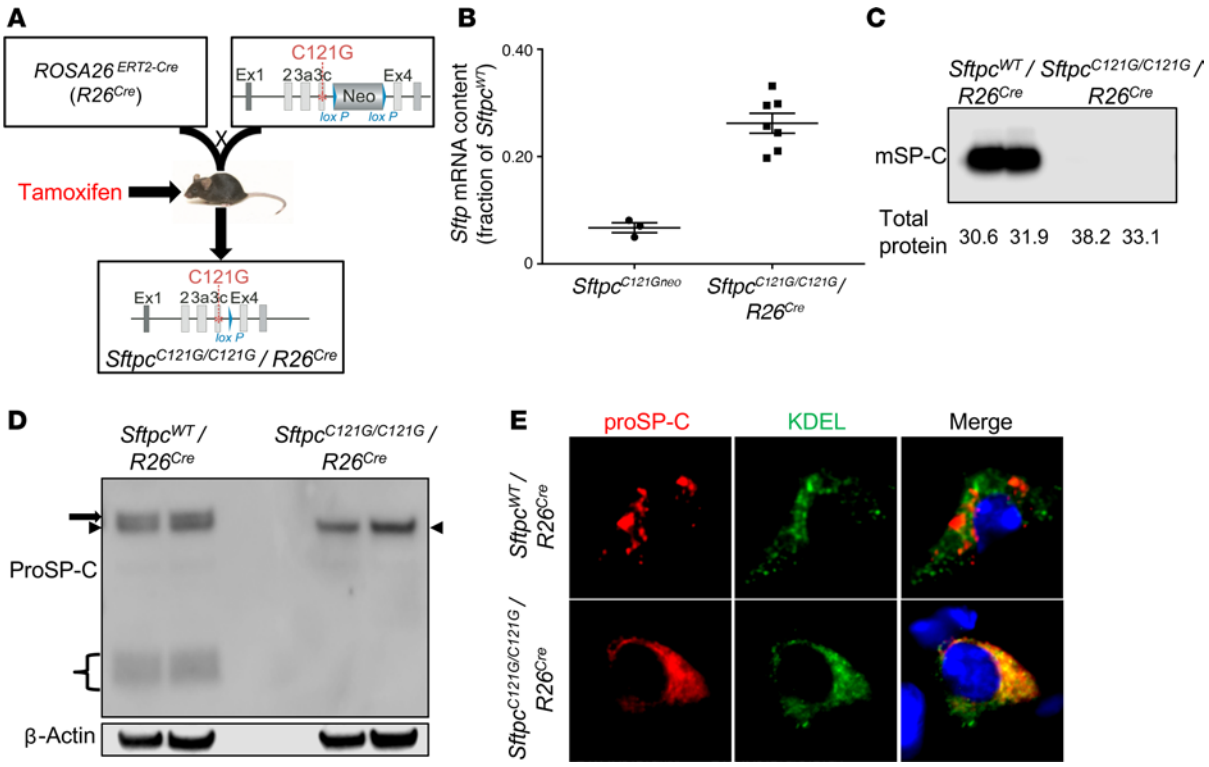

Figure 3. In vivo inducible expression of the *Sftpc*^{C121G} mutation in adult mice causes an ER-retained SP-C pro-protein. (**A**) Strategy for generation of tamoxifen-inducible mice in which tamoxifen treatment of the *Sftpc*$^{C121G/C121G}$ *R26*^{Cre} line results in removal of an inhibitory intronic PGK-neo cassette. (**B**) qRT-PCR analysis for *Sftpc* expression in purified AT2 cells from homozygous *Sftpc*$^{C121Gneo/C121Gneo}$ and *Sftpc*$^{C121G/C121G}$ *R26*^{Cre} mice at 7 days after treatment with tamoxifen. Data normalized to 18S RNA are expressed as *Sftpc* mRNA as a fraction of *Sftpc*^{WT} *R26*^{Cre} mice. (**C**) Western blotting of BALF large aggregate fraction from *Sftpc*$^{C121G/C121G}$ *R26*^{Cre} and *Sftpc*^{WT} *R26*^{Cre} mice on day 7 after tamoxifen showing the absence of mature SP-C (mSP-C) in the *Sftpc*$^{C121G/C121G}$ *R26*^{Cre} mice. (**D**) Western blotting of AT2 cell lysates from *Sftpc*^{WT} *R26*^{Cre} or *Sftpc*$^{C121G/C121G}$ *R26*^{Cre} mice 7 days after tamoxifen shows *Sftpc*$^{C121G/C121G}$ *R26*^{Cre} AT2 cells with an ER retained pro-protein (arrowhead) without posttranslational palmitoylation (arrow) or processing intermediates (brackets) observed in *Sftpc*^{WT} *R26*^{Cre} AT2 cells. (**E**) Double-label immunofluorescence staining of whole lung sections for proSP-C (red) and the ER marker KDEL demonstrates reticular proSP-C staining with significant colocalization with KDEL in *Sftpc*$^{C121G/C121G}$ *R26*^{Cre} mice, compared with the punctate pattern of proSP-C staining distinct from KDEL observed in the *Sftpc*^{WT} *R26*^{Cre} mice (original magnification, ×60).

ATF4 and its downstream target CCAAT/enhancer-binding protein homologous protein (CHOP) (Figure 4C). Interrogation of the ATF6 pathway revealed a marked decrease in the ATF6 P90 precursor band in *Sftpc*^{C121G} AT2 cells (Figure 4C).

While initiation of UPR signaling is viewed as an adaptive cellular response, sustained overactivation can cause deleterious responses such as apoptosis, a feature of the epithelium in both sporadic and *SFTPC* mutation–related ILD (26, 37, 38). Previously, we have shown that in vitro expression of *SFTPC* BRICHOS mutations induces apoptosis via multiple UPR pathways, including ATF4/CHOP and IRE1/JNK (14). Double-label fluorescence immunohistochemistry of lung sections for proSP-C and cleaved caspase-3 at 7 days after tamoxifen treatment revealed a significant increase in the apoptotic index, with 9.4% ± 1.7% (mean ± SD, $n = 4$) AT2 cells undergoing apoptosis in the *Sftpc*$^{C121G/C121G}$ *R26*^{Cre} lungs compared with 1.6% ± 0.5% (mean ± SD, $n = 4$) in controls ($P = 0.001$) (Figure 4F). Thus, *Sftpc*^{C121G} expression induced the UPR and produced an ER stress, proapoptotic AT2 cell phenotype.

Expression of the Sftpc^{C121G} *mutation causes early morbidity and mortality from lung injury and AT2 cell–driven polycellular alveolitis. Sftpc*$^{C121G/C121G}$ *R26*^{Cre} mice demonstrated tamoxifen dose–dependent morbidity and mortality. At a dose of 350 mg/kg tamoxifen, the mice developed weight loss starting 7 days after tamoxifen treatment, with a nadir of 84.8% ± 9.6% (mean ± SD, $n = 13$) from baseline at 13 days (Figure 5A) in association with 40% early mortality (Figure 5B). Lower doses were nonfatal, and a higher dose (600 mg/kg) was 100% fatal (Supplemental Figure 4). The weight loss and death were commensurate with hypoxemia (Figure 5C) and increased BALF total protein (Figure 5D). Histologically, the *Sftpc*$^{C121G/C121G}$ *R26*^{Cre} mice developed acute, diffuse lung injury by day 14 (Figure 5E).

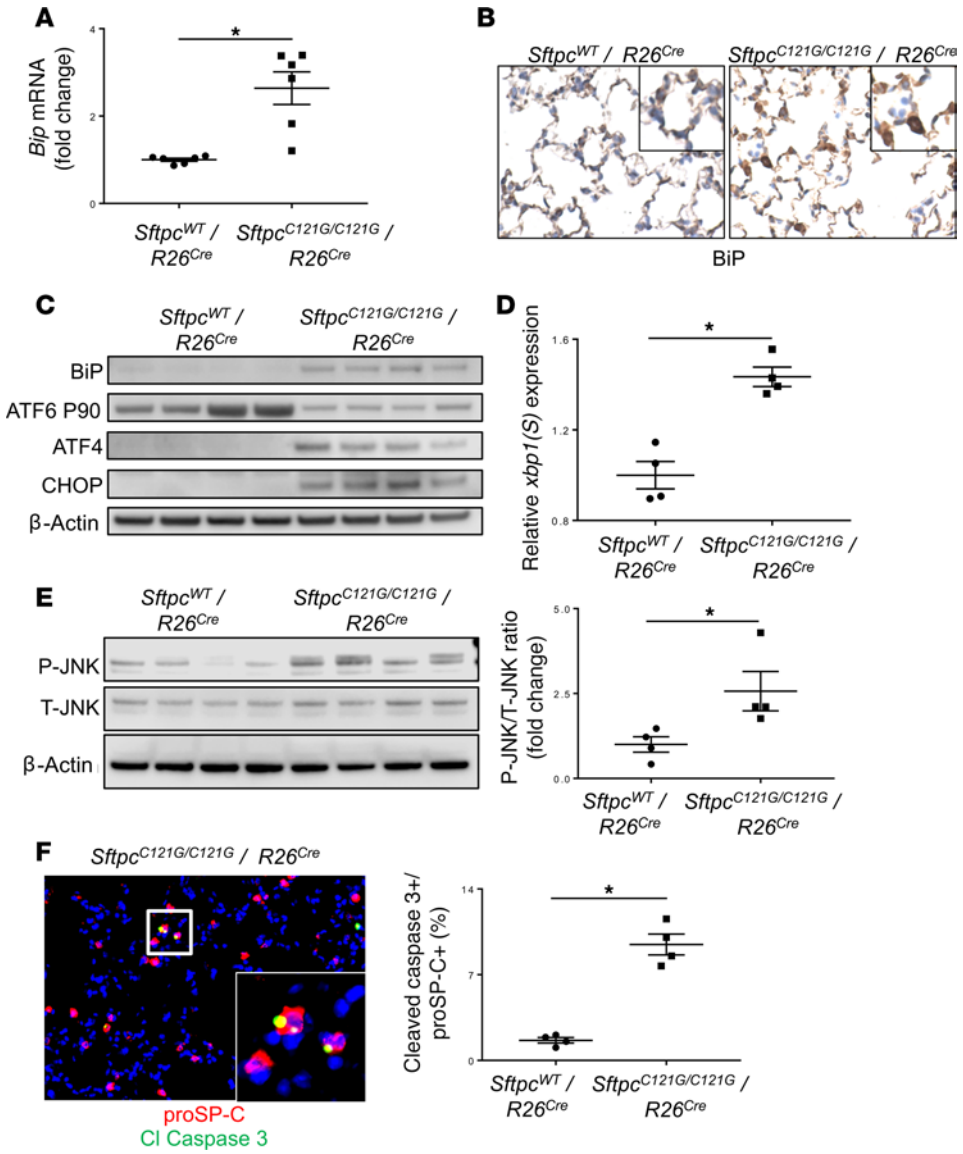

Figure 4. Expression of the SP-C C121G pro-protein causes activation of multiple epithelial ER stress pathways and induces AT2 cell apoptosis. (**A**) qRT-PCR for *BiP* expression in purified AT2 cells from *Sftpc*^{WT} *R26*^{Cre} controls and *Sftpc*$^{C121G/C121G}$ *R26*^{Cre} mice at 7 days after tamoxifen treatment. Data normalized to 18S RNA are expressed as fold change in *BiP* normalized to control mice. *$P < 0.05$ vs. control using unpaired 2-tailed *t* test. (**B**) Representative immunohistochemical staining for BiP in lung sections (magnification, ×20) from control and *Sftpc*$^{C121G/C121G}$ *R26*^{Cre} mice at 7 days after tamoxifen shows increased BiP staining in AT2 cells (inset magnification, ×60). (**C**) Western blotting of AT2 cell lysates at 7 days after tamoxifen for BiP, ATF6 (P90), ATF4, CHOP, and β-actin. (**D**) qRT-PCR for *XBP1* splicing ratio in AT2 cells at 7 days after tamoxifen shows an increase in the spliced fraction in *Sftpc*$^{C121G/C121G}$ *R26*^{Cre} AT2 cells compared with controls. *$P < 0.05$ vs. control using unpaired 2-tailed *t* test. (**E**) Western blot (left) of AT2 cell lysates at 7 days after tamoxifen for phosphorylated JNK (P-JNK), total JNK (T-JNK), and β-actin. Densitometry ratio (right) of P-JNK/T-JNK, reveals increase in P-JNK in *Sftpc*$^{C121G/C121G}$ *R26*^{Cre} mice compared with control. *$P < 0.05$ vs. control using unpaired 2-tailed *t* test. (**F**) Representative ×20 fluorescence micrograph from *Sftpc*$^{C121G/C121G}$ *R26*^{Cre} lung 7 days after tamoxifen stained with proSP-C (red) and cleaved caspase-3 (green) (left). Dot plots of double-positive (cleaved caspase-3$^+$/proSP-C$^+$) cells expressed as a percentage of total proSP-C$^+$ AT2 cells are shown with means and SEM (right). *$P < 0.05$ vs. control using unpaired 2-tailed *t* test.

The parenchymal lung injury was accompanied by polycellular alveolitis, with a substantial increase in total BALF cell counts beginning 7 days after tamoxifen treatment and peaking at 2 weeks (Figure 5F). BALF cytospins demonstrated multiphasic inflammatory cell alveolitis, with an early and sustained increase in macrophage/monocyte lineages beginning 7 days after tamoxifen, a rise in neutrophils starting 7 days after tamoxifen and peaking by 2 weeks, and an increase in eosinophils at 2 weeks (Figure 5G and

Supplemental Table 1). This pattern of granulocyte alveolitis mirrored that found in the *Sftpc*^{I73T} model (10). Total lymphocytes also increased by day 14 and were sustained through 28 days, albeit at numbers 1 log fold less than the macrophage/monocyte and granulocyte cell populations. The inflammatory phenotype was dependent on *Sftpc*^{C121G} allele status, with mice heterozygous for the *Sftpc*^{C121G} allele (*Sftpc*$^{C121G/WT}$ *R26*^{Cre}) developing less-severe alveolitis 2 weeks after tamoxifen that was sustained to 4 weeks, but in the absence of weight loss or early mortality (Supplemental Figure 5).

To define the effector cell populations that precede the overt alveolitis, flow cytometry analysis of whole lung tissue was performed 3 days after tamoxifen treatment using the gating strategy shown in Supplemental Figure 6. By this algorithm, an early decrease in the relative percent of SigF^{+}CD11b^{-} resident alveolar macrophages was found (Figure 5H), commensurate with an influx of inflammatory CD11b^{+}Ly-6C^{hi} monocytes (Figure 5I), a population recently implicated in fibrotic lung remodeling (39, 40).

In order to define the potential mediators of effector cell recruitment, BALF samples at early- and late-stage alveolitis were analyzed by multiplex assay and ELISA (Supplemental Table 2). CCL2 (MCP1), CCL17 (TARC), and CCL7 (MCP-3) were found to be increased in the BALF of *Sftpc*$^{C121G/C121G}$ *R26*^{Cre} mice compared with *Sftpc*^{WT} *R26*^{Cre} controls at the early time point (Figure 6A). Importantly, increases in AT2 cell mRNA expression of *Ccl2*, *Ccl17*, and *Ccl7* occurred by 7 days, suggesting that this cellular compartment is a potential source of these cytokines (Figure 6B). Notably, although elevations in cytokine levels for CCL2, CCL17, and CCL7 were not statistically significant 3 days after tamoxifen treatment, there was a 2.6 ± 1.2– (mean ± SD, $n = 4$, $P = 0.01$), 3.1 ± 1.0– (mean ± SD, $n = 4$, $P = 0.01$), and 3.0 ± 0.5– fold (mean ± SD, $n = 4$, $P = 0.005$) increase in AT2 cell mRNA expression, respectively. These data coupled with the early influx of inflammatory monocytes suggest that local elaboration of these cytokines may contribute to the recruitment.

In addition to the monocyte/macrophage lineages, *Sftpc*^{C121G} AT2 cells also contributed to granulocyte recruitment. *Sftpc*^{C121G} AT2 cells had increased mRNA expression of *Ccl11* and *Il5* compared with control AT2 cells, and BALF showed an increase in the corresponding eosinophil chemokines CCL11 (eotaxin) and IL-5 at 1 week after tamoxifen treatment (Supplemental Figure 7). This occurred in the absence of detectable increases in the canonical Th2 cytokines IL-4 and IL-13. Additionally, a 10-fold increase in *Sftpc*^{C121G} AT2 cell expression of the murine homolog to *IL8* (neutrophil chemoattractant KC [*Cxcl1/GroA*]) occurred and was also reflected by elevated BALF KC/CXCL1 content at 1 week after tamoxifen (Supplemental Figure 7). There was also a significant increase in BALF IL-6, which along with IL-8 has been posited as a biomarker for acute exacerbations of ILD (AE-ILD) (41, 42) (Supplemental Table 2). In contrast to IL-8, there was no increase in *Il6* mRNA expression in *Sftpc*^{C121G} AT2 cells, suggesting a non–AT2 cell source of IL-6 such as the distal lung mesenchyme (43). In total, *Sftpc*^{C121G} AT2 cells were an early source of cytokines that mediate the recruitment of multiple immune effector cell populations and an important contributor to the early lung inflammatory phenotype.

High-dimensional proteomic screen of a pediatric SFTPC BRICHOS mutation cohort translationally overlaps with the Sftpc^{C121G} *cytokine profile*. The translational relevance of the *Sftpc*^{C121G} model was assessed in a human pediatric cohort of patients with ChILD. Five patients with ChILD carrying *SFTPC* BRICHOS mutations and 9 control subjects underwent BALF analysis. Subjects with *SFTPC* BRICHOS mutations had an increase in total BALF cell count and an increase in the percentage of BALF eosinophils compared with controls (Supplemental Table 3). BALF supernatants were analyzed using a SOMAscan aptamer proteomics platform for 1129 proteins, which identified 7 proteins increased in the *SFTPC* BRICHOS subjects' BALF that met conservative significance criteria ($P < 0.001$; difference greater than 1 on a $\log_2$ scale). Five of these proteins were associated with the recruitment of immune cells (Figure 7A). Three were also increased in the *Sftpc*^{C121G} model (Figure 6A) and have been well described in adult ILD cohorts (44–49): CCL2 (MCP-1), CCL17 (TARC), and CCL7 (MCP-3) (Figure 7, B–D). All 3 of these cytokines are associated with macrophage/monocyte recruitment, the initial effector population identified in the *Sftpc*$^{C121G/C121G}$ *R26*^{Cre} lungs.

Expression of Sftpc^{C121G} *results in the development of spontaneous fibrotic lung remodeling*. The lung injury and morbidity observed 2 weeks after tamoxifen treatment in the *Sftpc*$^{C121G/C121G}$ *R26*^{Cre} mice was followed by partial recovery of weight loss and a decrease in BALF cell counts. However, 4 weeks after tamoxifen treatment, lung sections from *Sftpc*$^{C121G/C121G}$ *R26*^{Cre} mice demonstrated spatially heterogeneous areas of dense trichrome-positive parenchymal remodeling (Figure 8, A and B) in association with the accumulation of smooth muscle actin–positive (SMA-positive) cells adjacent to hyperplastic AT2 cells (Figure 8C). There was also a demonstrable quantitative increase in lung collagen deposition, measured as both soluble collagen content of the lungs by Sircol assay (Figure 8D) and as fibrillar collagen content assessed

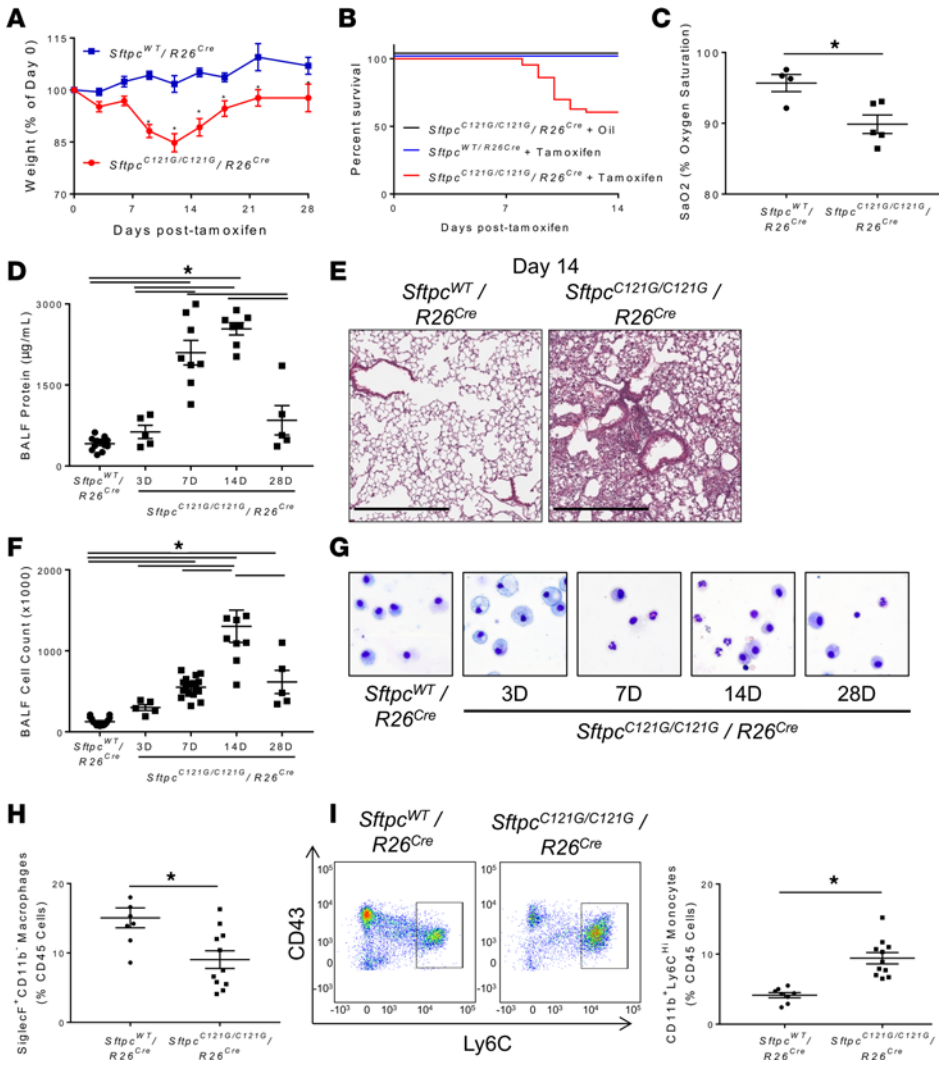

Figure 5. Expression of mutant *Sftpc*^{C121G} causes lung injury with polycellular alveolitis. (**A**) Weight loss curve in surviving *Sftpc*$^{C121G/C121G}$ *R26*^{Cre} mice and *Sftpc*^{WT} *R26*^{Cre} controls treated with tamoxifen. *$P < 0.05$ vs. control group using unpaired 2-tailed *t* test. (**B**) Kaplan-Meier survival curve of *Sftpc*$^{C121G/C121G}$ *R26*^{Cre} mice treated with tamoxifen ($n = 43$) or vehicle (oil) ($n = 16$) and *Sftpc*^{WT} *R26*^{Cre} mice treated with tamoxifen ($n = 32$). End points were defined as death or body weight <75% on 2 consecutive days. $P < 0.001$ by log-rank (Mantel-Cox) test. (**C**) Pulse oximetry of *Sftpc*$^{C121G/C121G}$ *R26*^{Cre} mice and controls 7 days after tamoxifen. *$P < 0.05$ vs. control using unpaired 2-tailed *t* test. (**D**) BALF protein content following tamoxifen. Controls represent pooled samples from all 4 time points. *$P < 0.05$ by 1-way ANOVA with post hoc Tukey's test. (**E**) Representative ×10 magnification H&E histology at 14 days after tamoxifen. Scale bars: 500 µm. (**F**) Dot plots with mean and SEM of BALF cell count following tamoxifen. Controls represent pooled samples from all 4 time points. *$P < 0.05$ by 1-way ANOVA with post hoc Tukey's test. (**G**) Representative Giemsa-stained BALF cytospins from control and *Sftpc*$^{C121G/C121G}$ *R26*^{Cre} mice after tamoxifen (magnification, ×20). (**H**) Dot plots with mean and SEM of percentage of total lung digest immune cells (CD45$^+$) that were alveolar macrophages (SiglecF$^+$CD11b$^-$) at 3 days after tamoxifen. *$P < 0.05$ vs. control using unpaired 2-tailed *t* test. (**I**) Representative control and *Sftpc*$^{C121G/C121G}$ *R26*^{Cre} flow cytometry gating for CD11b$^+$Ly6C^{hi} monocytes at day 3 after tamoxifen (left). Dot plots with mean and SEM of percentage of total lung digest immune cells (CD45$^+$) that were CD11b$^+$Ly6C^{hi} monocytes. *$P < 0.05$ vs. control using unpaired 2-tailed *t* test.

by picrosirius red staining (Figure 8E). Additionally, total lung *Col1a1* and *Col3a1* gene expression was increased (Figure 8F), demonstrating active fibrotic remodeling 4 weeks after tamoxifen. The observed structural and biochemical changes correlated with restrictive impairment on lung mechanics, with flow volume curves exhibiting a 30% decline in static lung compliance compared with control (Figure 8G). Quantification of AT2 cells in serial lung sections identified by either proSP-B staining or proSP-C staining at 4 weeks after tamoxifen demonstrated a 23.3% ± 4.0% (mean ± SD, $n = 3$) and 27.5% ± 3.8% (mean ± SD, $n = 3$) decline in AT2 cell number from 1 week after tamoxifen, respectively, with heteroge-

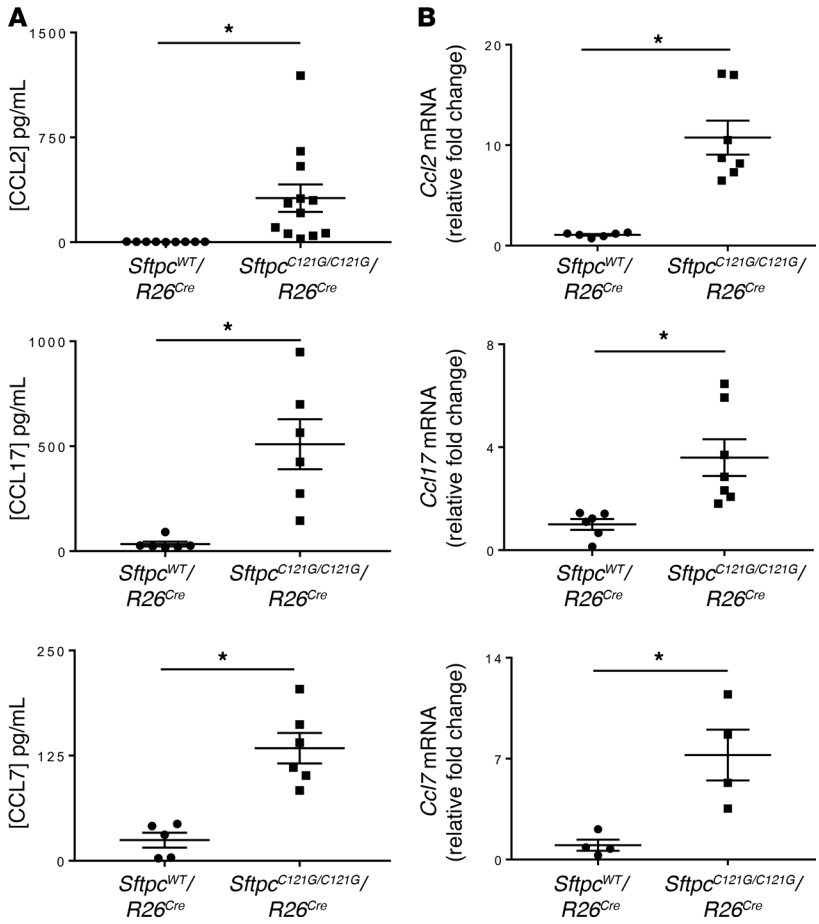

Figure 6. *Sftpc*^{C121G} AT2 cells are a source of cytokines associated with macrophage/monocyte recruitment. (**A**) Dot plots with mean and SEM of BALF CCL2 (top), CCL17 (middle), and CCL7 (bottom) protein in *Sftpc*$^{C121G/C121G}$ *R26*^{Cre} mice and *Sftpc*^{WT} *R26*^{Cre} controls 7 days after tamoxifen treatment determined by Luminex assay (CCL2 and CCL17) and ELISA (CCL7). *$P < 0.05$ versus controls by 1-way ANOVA (see Supplemental Table 2), followed by post hoc Tukey's test. (**B**) qRT-PCR determination of *Ccl2* (top), *Ccl17* (middle), and *Ccl7* (bottom) mRNA expression in AT2 cells 7 days following tamoxifen. Dot plots with mean and SEM. *$P < 0.05$ vs. control using unpaired 2-tailed *t* test.

neous regions of higher and lower AT2 cell density (Supplemental Figure 8). Given the concordance in cell number quantified by each AT2 cell–specific marker, it appeared that at 4 weeks after tamoxifen, the majority of AT2 cells continued to express *Sftpc*^{C121G}.

An increase in the potent antiinflammatory and profibrotic mediator TGF-β1 preceded the appearance of the fibrotic remodeling and was commensurate with the resolution of inflammation at 2 weeks after tamoxifen treatment (Figure 8H). *Sftpc*^{C121G} AT2 cells were a contributing source of TGF-β1, with increases in both gene expression of *Tgfb1* (Figure 8G) and AT2 cell TGF-β1 staining (Supplemental Figure 9). Concurrently, MMP-7, a component of the profibrotic milieu that was elevated in *SFTPC* BRICHOS patients' BALF (Supplemental Figure 10A) and has been described in adults with IPF (50), was also increased in the *Sftpc*$^{C121G/C121G}$ *R26*^{Cre} mouse BALF during this transitional period to fibrosis (Supplemental Figure 10B). Thus, following the resolution of the alveolitis, the *Sftpc*$^{C121G/C121G}$ *R26*^{Cre} mice express fibrotic mediators and biomarkers found in ChILD and ILD, and develop spontaneous fibrotic lung remodeling with a substantial restrictive impairment in respiratory mechanics.

Discussion

ER stress is a recognized pathway in the pathogenesis of fibrosis in multiple organs, including heart, kidney, liver, and lung (51). AT2 cell ER stress is also an appreciated feature of the epithelium in sporadic ILD and IPF (17, 52). There are multiple postulated etiologies for this, including exogenous factors such as air pollution, cigarette smoke exposure (52), and chronic viral infections (53, 54). Additionally, it is

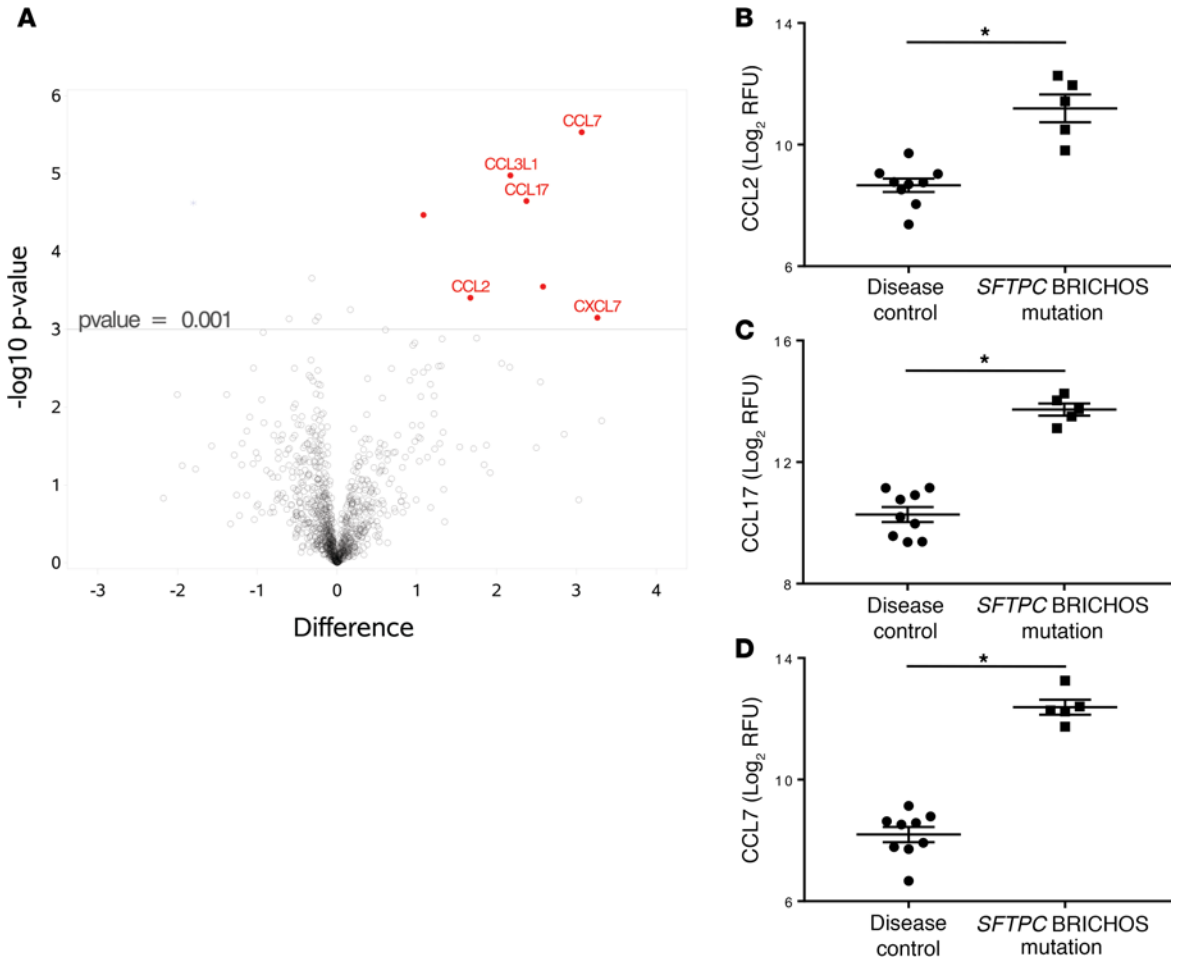

Figure 7. Pediatric *SFTPC* BRICHOS mutation patients elaborate multiple cytokines associated with macrophage/monocyte recruitment found in *Sftpc*^{C121G} mice. (**A**) Volcano plot of SOMAscan proteomics platform analysis of BALF from *SFTPC* BRICHOS mutations cases (n = 5) and disease control (n = 9). Minus $\log_{10}$–transformed P value on y axis, and $\log_2$ difference on x axis. Conservative selection of cytokines associated with immune cell recruitment with relative florescence units (RFU) difference greater than 1 on a $\log_2$ scale and $P < 0.001$ (shown in red). (**B**–**D**) Individual dot plots of mean ± SEM $\log_2$ RFU for (**B**) CCL2, (**C**) CCL17, and (**D**) CCL7. *$P < 0.05$ for *SFTPC* BRICHOS mutation cases versus disease control using unpaired 2-tailed t test.

hypothesized that epithelial ER stress can arise from dysfunctional epithelial proteostasis in an aging or senescent epithelium (55–57). However, in vivo modeling to derive proof of concept linking AT2 cell ER stress and fibrotic lung remodeling has been elusive. Here we present a model that provides evidence that AT2 expression of a disease-associated *SFTPC* BRICHOS mutation is sufficient to activate the UPR and produce spontaneous lung inflammation and fibrotic remodeling. Thus, AT2 cell ER stress and our *Sftpc*^{C121G} model fit within the growing paradigm that disturbance in epithelial cell quality control drives fibrotic lung disease (7, 58). In support of this, we recently reported on the non-BRICHOS *Sftpc*^{I73T} mouse model, where expression of this trafficking mutation causes defective AT2 cell macroautophagy in the absence of ER stress, with resultant spontaneous inflammation and fibrotic lung remodeling (10). These two models taken together strongly support the notion that distinct endophenotypes of AT2 cell dysfunction may each contribute to ChILD and ILD through both overlapping and distinct pathways.

Previous in vivo *SFTPC* BRICHOS mutation models have been limited by technical difficulties with the control of relevant gene dosages. Constitutive *SFTPC*$^{\Delta exon4}$ mutation expression in mice resulted in dose-dependent disrupted lung morphogenesis with prenatal lethality (18). While that model recapitulated the cell biology of the *SFTPC* mutation and established a toxic gain of function for *SFTPC* BRICHOS mutations, the transgenic expression of this highly aggregation-prone mutation using a human *SFTPC* promoter fragment is the likely cause of the severe developmental phenotype, limiting its translational relevance. Whereas the *SFTPC*$^{\Delta exon4}$ model demonstrated a severe developmental phenotype, the inducible transgenic

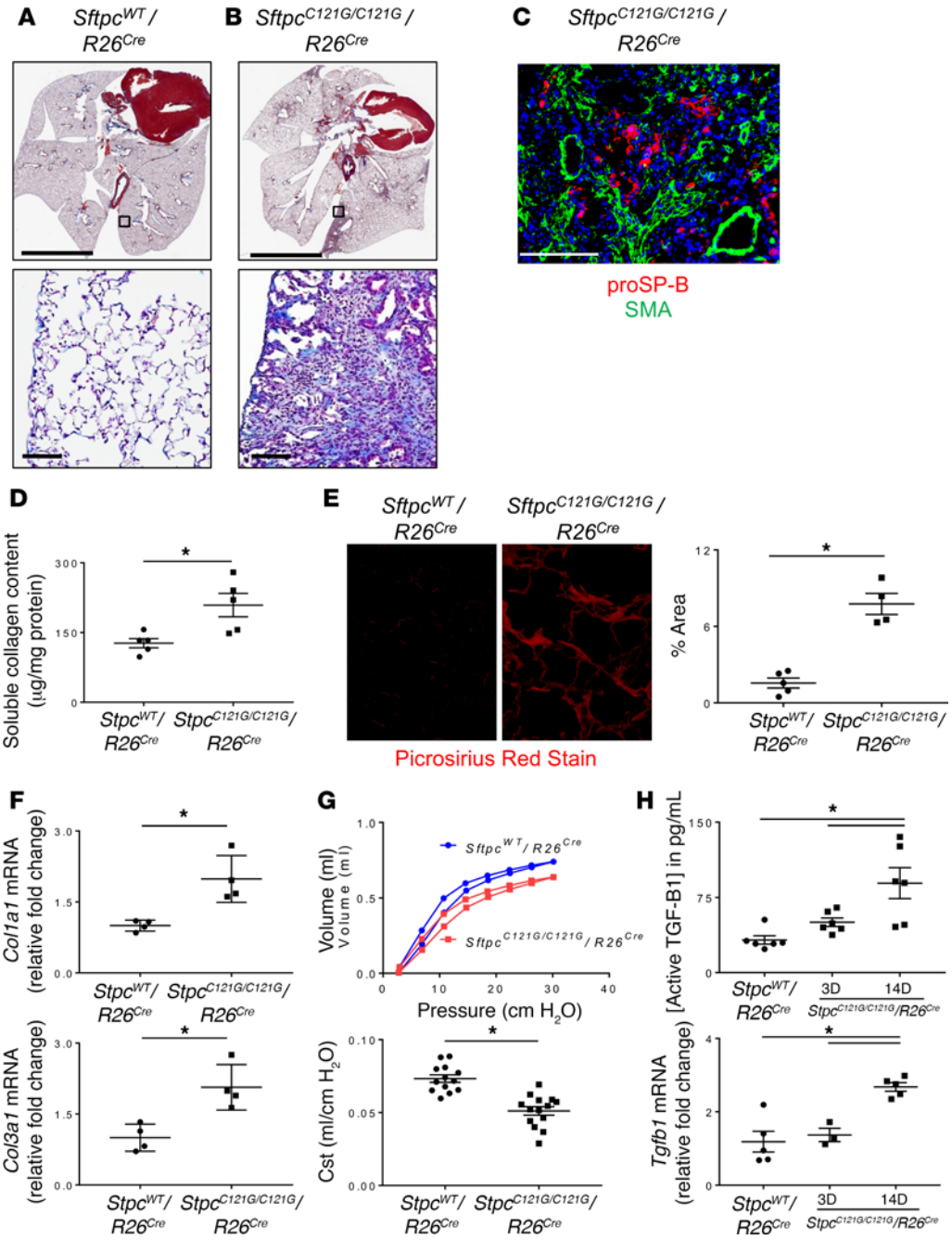

Figure 8. Mice expressing the *Sftpc*^{C121G} mutation develop spontaneous fibrotic lung remodeling. Representative trichrome staining of *Sftpc*^{WT} *R26*^{Cre} (**A**) and *Sftpc*$^{C121G/C121G}$ *R26*^{Cre} (**B**) lung section 28 days after tamoxifen treatment showing patchy areas of fibrotic remodeling in *Sftpc*$^{C121G/C121G}$ *R26*^{Cre} mice. Scale bars in ×0.5-magnification upper panels: 5 mm; scale bars in ×10-magnification lower panels: 100 μm. (**C**) Double-label immunohistochemistry of *Sftpc*$^{C121G/C121G}$ *R26*^{Cre} lungs showing proSP-B$^+$ AT2 cells (red) with adjacent smooth muscle actin (SMA; green) myofibroblasts (magnification, ×20; scale bar: 100 μm). (**D**) Soluble collagen in right lung homogenates measured by Sircol assay. Shown are dot-plots with mean and SEM. *P < 0.05 vs. control using unpaired 2-tailed t test. (**E**) Left: Representative picrosirius red–stained ×20-magnification fields. Right: Quantification performed using ImageJ expressed as picrosirius staining as percentage of section area with dot plots, and mean and SEM shown. *P < 0.05 vs. control using unpaired 2-tailed t test. (**F**) Whole lung expression of *Col1a1* (top) and *Col3a1* (bottom) mRNA assayed by qRT-PCR and expressed as fold change from controls. Dot plots and mean and SEM are shown. *P < 0.05 vs. control using unpaired 2-tailed t test. (**G**) Pooled flow volume loops (top) (n = 10) and calculated static compliance (Cst; bottom) from pulmonary function testing at 28 days after tamoxifen. *P < 0.05 vs. control using unpaired 2-tailed t test. (**H**) Top: Active TGF-β1 levels in BALF at indicated times after tamoxifen were measured using Luminex; shown are dot plots with mean and SEM. *P < 0.05 vs. control using unpaired 2-tailed t test. Bottom: qRT-PCR for *Tgfb1* mRNA expression in AT2 cells isolated at 3 and 14 days after tamoxifen. Data expressed as fold change from control group are presented as dot plots with mean and SEM shown. *P < 0.05 versus controls by 1-way ANOVA with post hoc Tukey's test.

SFTPC^{L188Q} model lacked a spontaneous phenotype, but had increased susceptibility to bleomycin-induced fibrotic remodeling (19). This model was limited by both low (10% of WT) *SFTPC*^{L188Q} mRNA expression and the observation in vitro that this mutated pro-protein was less aggregation prone than other BRICHOS mutations, suggesting a less-severe cellular response to this isoform (59).

Based on the importance of the disulfide cysteine bonds in the BRICHOS domain for primary folding and processing (20) and our in vitro modeling of C121 mutant proSP-C isoforms (Figure 1), we selected an *Sftpc* mutation that we anticipated would cause significant ER stress. We developed a hypomorphic founder line that expressed low *Sftpc*^{C121G} mRNA and no detectable mutant proSP-C, and lacked a spontaneous phenotype. This was in contrast to the hypomorphic *Sftpc*^{I73T} line, where an age-dependent lung phenotype developed in parallel with the steady accumulation of mutant proSP-C isoforms due to their mistrafficking and evasion of proteasomal quality control (10). In contrast, SP-C BRICHOS mutations are substrates for proteasomal degradation, limiting their expression until transcription/translation exceeds proteasomal capacity (15), which likely accounts for the difference in protein expression in the two hypomorphic models. Since the founder *Sftpc*^{C121G} line failed to generate a spontaneous phenotype, we developed complimentary models with sufficient gene expression to recapitulate various aspects of the human lung phenotype. Constitutive heterozygous *Sftpc*^{C121G} expression allowed both proof of concept of the dominant negative effect of the mutant pro-protein on WT proSP-C processing (Figure 2, B and C), and a neonatal lung phenotype that mimicked clinical cases of ChILD with *SFTPC* BRICHOS mutations (Figure 2, D–F). However, in the adult inducible model we discovered that heterozygous *Sftpc*^{C121G} expression was insufficient to develop a robust phenotype. This was similar to what was described in the *Sftpc*^{I73T} model and likely reflects that either the developing epithelium is more sensitive to the mutated isoforms or that low *Sftpc* ^{C121G} transcription in the heterozygous adult model was inadequate to produce sufficient mutant pro-protein capable of generating a toxic gain of function.

To overcome the limitation of low *Sftpc* mRNA in the adult inducible model, we selected homozygous *Sftpc*^{C121G} expression with inducible Cre-driven expression under a strong *Rosa26* promoter. While using this Cre-ERT2 system limited the ability to perform AT2 cell lineage tracing experiments (as could be performed with *Sftpc*^{ERT2Cre}), it did produce a gene dose level closer to predicted levels for heterozygous *SFTPC* BRICHOS mutation patients, and was capable of inducing a stronger ER stress cellular phenotype. Thus, by modulating gene dose in both the constitutive and inducible in vivo models, we were able to produce lung phenotypes that recapitulated the spectrum of pediatric and adult *SFTPC* BRICHOS–associated ILD, providing proof of concept linking AT2 cell ER stress and spontaneous fibrotic lung remodeling.

The translational relevance of this model was supported by the discovery of multiple biomarkers associated with human ILD in the *Sftpc*^{C121G} BALF. These included MMP-7, which is a well-described marker of fibrotic tissue remodeling in IPF (60) and was identified both in our pediatric proteomic analysis (Supplemental Figure 10) and in the *Sftpc*^{I73T} model. Additionally, we identified IL-6 and IL-8 in *Sftpc*^{C121G} BALF during the inflammatory phase of the model (Supplemental Table 2), consistent with analyses of patient samples during AE-ILD that have identified increased plasma levels of IL-8 and IL-6 as biomarkers associated with worse prognosis (41, 42).

The role of inflammation and immune effector cell populations in ILD is an area of ongoing research, but the importance of this is highlighted clinically by AE-ILDs. Key cellular features of acute exacerbations include epithelial injury and apoptosis, and the recruitment of a mixed granulocytic cell population (61, 62). In this regard, the AT2 cell apoptosis (Figure 4F), alveolitis (Figure 5, F and G), and subsequent fibrotic remodeling (Figure 8) in our model recapitulate the human disease. We found that the *Sftpc*^{C121G} AT2 cell was responsible for early cytokine production associated with immune cell recruitment (Supplemental Figure 7). This corroborated previous in vitro studies where expression of *SFTPC* BRICHOS mutations caused the secretion of cytokines associated with immune cell recruitment (13, 14). The relationship between ER stress and inflammation has been an active area of study in multiple organ systems, including in the pathogenesis of diabetes in the pancreatic B cell (63), hepatic steatosis liver disease (64, 65), and vascular atherosclerosis (66). However, that the *Sftpc*^{I73T} model had both a similar immune cell ontogeny and overlapping AT2 cell–produced cytokines suggests that AT2 cell ER stress per se may not underlie the effector cell recruitment (10), but rather that distinct AT2 cell dysfunction endophenotypes converge to produce a common cytokine profile. The regulation of both this immune cell recruitment and then the transition to resolution of alveolitis represent two important areas of future research requiring additional understanding of epithelial-immune cell crosstalk.

Preceding the overt alveolitis, we identified the recruitment of monocyte/macrophage effector cells (Figure 5I and Figure 6). $CD11b^{+}Ly6C^{hi}$ monocytes have been experimentally shown to participate in the development of fibrotic lung disease in exogenous models of injury/repair such as bleomycin and were found to be an early immune population recruited in the $Sftpc^{I73T}$ model (10, 39, 67). Our models of spontaneous injury suggest that $CD11b^{+}Ly6C^{hi}$ monocytes are recruited to replenish the alveolar macrophage niche, which is consistent with recent evidence showing monocyte-derived alveolar macrophages as a key fibrogenic subset (39). We found the monocyte/macrophage cytokine CCL2/MCP-1 in $Sftpc^{C121G}$ BALF, which has previously been identified in fibrotic lung disease and preclinical models (10, 48, 49, 68–70). However, we also uncovered elevated levels of CCL17/TARC and CCL7/MCP-3, cytokines with overlapping functional redundancies with CCL2/MCP-1. All 3 of these cytokines were elaborated in the pediatric proteomic analysis (Figure 7), proving a translational context for this discovered redundancy, which may account for the phase II clinical trial failure of pharmacologic MCP-1 neutralization as a therapy in IPF (71).

There are multiple possible mechanisms by which fibrosis develops in this model. During the inflammatory phase of the model, there is AT2 cell apoptosis, which has been associated with the development of fibrosis in AT2 cell ablation models (72). However the 20%–30% decline in AT2 cell number we observed in this model at 4 weeks after tamoxifen treatment was a degree of apoptosis found to be insufficient to induce spontaneous fibrosis in multiple AT2 cell ablation models (73, 74). Alternatively, our data show that the $Sftpc^{C121G}$ AT2 cell is a source of the potent fibrotic mediator TGF-β1 (Figure 8G), although the true contribution of TGF-β1 to the development of fibrosis in this model would require TGF-β1 depletion. In the lung there has been limited mechanistic work on the link between epithelial ER stress and TGF-β1 (57, 75). However, UPR pathways such as ATF4/CHOP have been implicated in TGF-β1 production in epithelial injury models of liver and kidney fibrosis (76, 77). That AT2 cell *Tgfb1* expression in the $Sftpc^{C121G}$ model increased 2 weeks after tamoxifen treatment demonstrates a temporal sequence of events, with early AT2 cell proinflammatory cytokine production followed by a transition to the release of antiinflammatory and profibrotic TGF-β1. The regulation of this phenotypic transition may provide additional insights into the accelerated fibrosis that occurs during recovery from an AE-ILD.

In conclusion, the $Sftpc^{C121G}$ model provides proof of principle for the role of AT2 cell ER stress in pediatric ChILD and adult ILD. We have demonstrated that $Sftpc^{C121G}$ AT2 cells are a source of multiple relevant chemokines/cytokines associated with the recruitment of significant effector cell populations supporting a proximal position for the AT2 cell in the pathway to fibrosis. While the precise UPR pathways responsible for the expression of these cytokines and the fibrotic mediator TGF-β1 would require genetic or pharmacologic inhibition, this model represents a new tool for therapeutic intervention studies such as these. The translational relevance of the model is further supported by the identification of these cytokines and other biomarkers in the high-dimensional BALF proteomic analysis of patients with ChILD from *SFTPC* BRICHOS mutations. The $Sftpc^{C121G}$ model thus connects AT2 cell dysfunction manifesting as ER stress with lung inflammation and aberrant lung remodeling, supporting its role as a novel and relevant preclinical model.

Methods

Supplemental Methods are available online with this article.

Mouse models. The $Sftpc^{C121Gneo}$ founder line was commercially produced (Genoway Inc.) using targeting vector–based embryonic stem cell electroporation transfection strategies to knock in coding sequences for the cysteine-to-glycine substitution at codon 121 into the endogenous mouse *Sftpc* locus (depicted in Supplemental Figure 1A). For constitutive removal of the lox-P flanked PGK-neo cassette from $Sftpc^{C121Gneo}$ allele in utero, homozygous $Sftpc^{C121Gneo/C121Gneo}$ female mice were bred to the heterozygous X-linked CMV-Cre recombinase line [strain B6.C-Tg(CMV-cre)1Cgn/J; stock 006054; The Jackson Laboratory] (25). For tamoxifen-inducible removal of PGK-neo from $Sftpc^{C121Gneo}$ alleles, the $Sftpc^{C121Gneo}$ founder line was crossed to the Rosa26-ERT2-Cre line [strain B6.129-Gt(ROSA)26Sortm1(cre/ERT2)Tyj/J; stock 008463; The Jackson Laboratory]. The progeny was backcrossed to homozygosity of the $Sftpc^{C121Gneo}$ allele and the $R26^{Cre}$ allele. All mouse strains and genotypes generated for these studies were congenic with C57BL/6J. Both male and female animals (aged 8–12 weeks) were utilized in tamoxifen induction protocols. Mice were housed under pathogen-free conditions in a barrier facility, and all experimental and breeding protocols were approved by the IACUC of the Perelman School of Medicine at the University of Pennsylvania.

Materials and reagents. Tamoxifen (non-pharmaceutical grade) was purchased from Sigma-Aldrich. Cytological slides were stained with Giemsa (GS500; Sigma-Aldrich). All other reagents were electrophoretic or immunological grade and purchased from either Sigma-Aldrich or Thermo Fisher Scientific.

Lung histology. Whole lungs were fixed by tracheal instillation of a 1.5% glutaraldehyde/1.5% paraformaldehyde mixture in 0.15 M HEPES buffer at a constant pressure of 25 cm H_2O and removed en bloc. Paraffin-embedded 6-μm lung sections were stained with H&E or Masson's Trichrome stain by the Pathology Core Laboratory of Children's Hospital of Philadelphia.

Immunohistochemistry and immunofluorescence. Immunohistochemical staining of paraffin-embedded lung sections was performed with primary antibodies at indicated dilutions as described in Supplemental Table 4. A commercial HRP-based method (Vectastain Elite Rabbit IgG ABC Kit PK6101, Vectastain DAB Substrate Kit SK410; Vector Laboratories) was used to visualize immunoreactivity. Following immunoreactivity staining, sections were counterstained with Mayer's hematoxylin.

Immunofluorescence staining of lung sections was performed with combinations of primary antibodies and secondary Alexa Fluor–conjugated anti-IgG (Supplemental Table 4). Images were visualized on an Olympus I-70 inverted fluorescence microscope, captured with a Hamamatsu 12-bit coupled-charged camera, and processed using Metamorph, version 7.8.4.0 (Universal Imaging).

Quantitative determination of proSP-C– and ProSP-C–positive cells was performed by fluorescence immunostaining of serial lung sections with anti–proSP-C and anti–proSP-B. Five consecutive ×20 images were obtained from 2 different lobes (10 peripheral lung fields per section), with manual counting followed by quantification of positive cells per field. Apoptotic AT2 cell index was determined using double-label fluorescence immunostaining of lung sections with anti–proSP-C and anti–cleaved caspase-3. Five consecutive ×20 images were obtained from 2 different lobes (10 peripheral lung fields per section). Apoptotic (percentage cleaved caspase-3/proSP-C double-positive cells per total proSP-C–positive cells) indices were determined by manual counting.

Picrosirius red staining. Staining for collagen was performed using the Picrosirius Red Stain Kit (Polysciences Inc.) according to the manufacturer's instructions. Following staining of lung sections, 5 consecutive ×20 images were obtained from 2 different lobes (10 peripheral lung fields per section without large airways) for analysis. Digital morphometric measurements were performed using ImageJ (NIH). The mean area of positive picrosirius staining of each lung field was expressed as a percentage of total section area (10, 78).

Quantification of lung collagen content. Total right lung acid soluble collagen content was determined using the Sircol assay (Biocolor Ltd.) according to the manufacturer's instructions and as previously described (69).

BALF collection and processing. BALF was collected from mice using 5 sequential 1-ml sterile saline lung lavages. 300-μl aliquots of each cell-free, first 1 ml of BALF return was removed and stored at –80°C for cytokine analysis. Cell pellets recovered from centrifugation of complete return were resuspended in 1 ml sterile saline, and total cell counts determined by a Z1 Coulter Counter (Beckman Coulter). Differential cell counts were obtained by manually quantifying cytospins of BALF cell pellets stained with modified Giemsa (Sigma-Aldrich, GS500). Large-aggregate surfactant fractions were prepared from cell-free BALF by centrifugation at 20,000 *g* for 60 minutes at 4°C as described previously (79). Total protein content of BALF, surfactant, cell lysate, and whole lung homogenate were assayed by the Bradford method (79).

Cytokine analyses. Aliquots of first-return, cell-free BALF were analyzed for levels of a panel of cytokines [CCL2, CCL11, IL-4, IL-13, IL-5, IL-6, GM-CSF, IL-1β, KC(GroA); panel MCYTOMAG-70K-9] using the Luminex (Luminex Corp.) multiplex platform analyzed by the Human Immunology Core at the Perelman School of Medicine. Active TGF-β1 and CCL17 (TARC) were measured separately, also using Luminex kits (panels TGFBMAG-64K and MECY2MAG-73K). For select cohorts, CCL7 was measured using an MCP-3 ELISA kit (BM6006INST, Invitrogen).

Mouse AT2 cell isolation. Mouse AT2 cells were isolated as previously reported (69). Briefly, a single-cell suspension was obtained by instilling Dispase (BD Biosciences) into perfused lungs, followed by mechanical dissociation with a McIlwain tissue chopper (Metrohm USA) and treatment with 20 μg/ml DNAase I (Sigma-Aldrich). Differential adherence on plastic culture dishes negatively selected mesenchymal cells. $CD45^+$ cells were depleted by negative selection using Dynabeads Untouched mouse T cells kit (11413D) and Dynabeads mouse DC enrichment kit (11429D, Thermo Fisher Scientific). Recovered cells were collected and flash frozen at –80°C. Purity was determined by immunostaining preparations adhered overnight to 10% Matrigel-coated coverslips using DAPI in combination with primary antisera

for proSP-C. Manual counts in five 20x fields per sample were done, and purity was defined as number of pro-SP-C$^+$ cells (AT2 cells) divided by total nuclei showing >95% purity (n = 4).

SDS-PAGE and immunoblotting. SDS-PAGE using Novex Bis-Tris gels (NP0301, Thermo Fisher Scientific) and immunoblotting of PVDF membranes with primary antibody (Supplemental Table 4) was performed. This was followed by species-specific HRP-conjugated secondary antibody and band detection by enhanced chemiluminescence (ECL2 80196 Thermo Fisher Scientific or WesternSure 926-95000, LI-COR Biotechnology) using a LiCor Odyssey Fc Imaging Station and quantified using the manufacturers' software.

Antibodies. A polyclonal proSP-C antiserum ("NPRO-SP-C") raised against rat proSP-C and polyclonal anti-proSP-B ("PT3") raised against bovine proSP-B were each produced in rabbits in-house and previously validated as published (80, 81). The other antibodies used for these studies were obtained from commercial sources (Supplemental Table 4).

RNA isolation and qRT-PCR. cDNA was prepared from RNA template purified from AT2 cell or whole lung RNA using the RETROscript Kit (Thermo Fisher Scientific). qRT-PCR was performed using Taq polymerase and TaqMan RT-PCR kits (Applied Biosystems/Thermo Fisher Scientific) with primer sets for mouse genes (listed in Supplemental Table 5) on an ABI Prism 7900 system and a QuantStudio 7 Flex Real-Time PCR System.

Multichannel flow cytometry. Tissue immune cell characterization was performed as previously described (10). Briefly, en bloc lungs were digested in DMEM + 5% FBS + 2 mg/ml Collagenase D (catalog 11088866001, Roche), passed through 70-μm nylon mesh to obtain single-cell suspensions, and then mixed with Gibco RBC Lysis Buffer (A10492-01, Thermo Fisher Scientific). Cell pellets were resuspended in PBS + 0.1% sodium azide and blocked with anti–mouse CD16/32 antibody (Fc block, eBiosciences), followed by incubation with antibody mixtures (or isotype controls) and conjugated viability dye (see Supplemental Table 6). Single-cell suspensions were then analyzed on an LSR Fortessa (BD Biosciences). They were then gated on viability and singlets and analyzed with FlowJo software (FlowJo LLC) based on a modification of the strategy of Misharin et al. (82) as previously published (10) (Supplemental Figure 6).

Pediatric SFTPC mutation cohort for comparative BALF proteomics. Clinically indicated flexible bronchoscopy was performed, and BALF was collected, processed, and stored in a standard fashion. Disease control subjects were defined as patients with pulmonary symptoms necessitating flexible bronchoscopy, including unexplained wheeze, cough, congestion, and recurrent pneumonia, but normal-appearing bronchoscopy. BALF cytology and microbiologic testing were performed as part of routine clinical care (83). Briefly, the area of lavage was selected by the pulmonologist performing the procedure, and in general was performed in areas where mucus had collected or where infiltrate was seen on chest imaging. Typically, 3 lavages were performed using sterile nonbacteriostatic saline at room temperature. Each lavage aliquot consisted of 1 ml per kilogram of body weight, with a maximum of 30 ml normal saline per lavage. After BALF collection, any excess fluid not required for clinical laboratory testing was processed for research study. Collected BALF was processed in a standard manner. It was initially centrifuged for 10 minutes at 250 x g at 4°C. The pellet was saved, and the supernatant was spun again for 20 minutes at 4000 x g at 4°C. The second pellet was saved. This supernatant was split in half, with half stored 0.5 ml aliquots at –70°C. The other half of the supernatant was treated with the protease inhibitors PMSF and EDTA to inhibit protease activity. The samples were frozen at –70°C for further study.

SOMAmer proteomic analysis. SOMAscan technology (84, 85) was used to simultaneously measure 1129 proteins from each sample at SomaLogic Inc. BALF was diluted with buffer to a standard protein concentration of 20 μg/ml, and 100 μl diluted BALF was equilibrated with a SOMAmers mix (Gold 2010). The SOMAmer mixture allowed for the detection and quantitation of 1129 protein aptamers simultaneously in each sample recorded as relative florescence units (RFU). Raw RFU were adjusted based on the individual dilution factor for each sample to reflect the initial protein amounts.

Statistics. For in vitro and in vivo studies, all data are presented as dot plots and group mean ± SEM unless otherwise indicated. Statistical analyses were performed with GraphPad Prism. Student's t test (1- or 2-tailed as appropriate) were used for 2 groups and multiple comparisons were done with ANOVA with post hoc testing as indicated; survival analyses were performed using log-rank test. In all cases, statistical significance was considered at P values less than 0.05.

For the pediatric BALF analysis, adjusted RFU were $\log_2$ transformed, and quantile normalization was used to obtain final values for analysis. RFU for each protein aptamer were compared univariately between groups using difference in $\log_2$ means and a 2-sample t test assuming unequal variances. Con-

servative selection of aptamers included the intersection set with a difference greater than 1 on $\log_2$ scale and a *P* value less than 0.001. This approach provides a balance between selecting aptamers with a large absolute change and significant *P* value.

Study approval. Mice were housed in pathogen-free facilities according to protocols approved by the IACUC of the Perelman School of Medicine at the University of Pennsylvania. For the pediatric proteomics data, the study was approved by the Colorado Multiple Institutional Review Board (nos. 99-113 and 10-0472). Informed consent was obtained from all subjects for sample collection and study enrollment. If the patient was a minor, informed consent was obtained from the subject's legal guardian. In subjects aged 12–17 years, informed assent was obtained.

Author contributions

MFB and SM developed the concept. MFB, SM, JK, YT, MK, and AV designed the experiments. YT, JK, and MK performed in vivo animal experiments; JK, AV, SJR, ACH, MCB, MFB, and SM performed in vitro experiments and end point analyses for in vivo studies; RRD and BDW designed the human cohort study and performed the analysis; MFB, JK, AV, RRD, and BDW analyzed data, generated figures, and interpreted results; JK and MFB drafted the manuscript; MFB, AV, MCB, JMS, and SM edited the manuscript. All authors reviewed and approved the final version prior to submission.

Acknowledgments

We thank Hasina Outtz-Reed for assistance with pulse oximetry measurements. We thank Edward E. Morrisey for helpful discussions. This work was supported by VA Merit Review 1I01BX001176 (MFB), NIH R01 HL119436 (MFB), and HL129150 (SM); JK and MCB are supported by NIH 2T32 HL007586. The content of this article does not represent the views of the US Department of Veterans Affairs or the United States Government.

Address correspondence to: Michael F. Beers, Pulmonary and Critical Care Division, University of Pennsylvania School of Medicine, Suite 216 Edward J Stemmler Hall, 3450 Hamilton Walk, Philadelphia, Pennsylvania 19104-5159, USA. Phone: 215.898.9106; Email: mfbeers@pennmedicine.upenn.edu.

1. Travis WD, et al. An official American Thoracic Society/European Respiratory Society statement: update of the international multidisciplinary classification of the idiopathic interstitial pneumonias. *Am J Respir Crit Care Med*. 2013;188(6):733–748.
2. Kurland G, et al. An official American Thoracic Society clinical practice guideline: classification, evaluation, and management of childhood interstitial lung disease in infancy. *Am J Respir Crit Care Med*. 2013;188(3):376–394.
3. Raghu G, Chen SY, Hou Q, Yeh WS, Collard HR. Incidence and prevalence of idiopathic pulmonary fibrosis in US adults 18-64 years old. *Eur Respir J*. 2016;48(1):179–186.
4. Soares JJ, et al. Childhood interstitial lung diseases: an 18-year retrospective analysis. *Pediatrics*. 2013;132(4):684–691.
5. Barkauskas CE, Noble PW. Cellular mechanisms of tissue fibrosis. 7. New insights into the cellular mechanisms of pulmonary fibrosis. *Am J Physiol, Cell Physiol*. 2014;306(11):C987–C996.
6. Selman M, Pardo A. Revealing the pathogenic and aging-related mechanisms of the enigmatic idiopathic pulmonary fibrosis. an integral model. *Am J Respir Crit Care Med*. 2014;189(10):1161–1172.
7. Mulugeta S, Nureki S, Beers MF. Lost after translation: insights from pulmonary surfactant for understanding the role of alveolar epithelial dysfunction and cellular quality control in fibrotic lung disease. *Am J Physiol Lung Cell Mol Physiol*. 2015;309(6):L507–L525.
8. Lawson WE, et al. Genetic mutations in surfactant protein C are a rare cause of sporadic cases of IPF. *Thorax*. 2004;59(11):977–980.
9. van Moorsel CH, et al. Surfactant protein C mutations are the basis of a significant portion of adult familial pulmonary fibrosis in a dutch cohort. *Am J Respir Crit Care Med*. 2010;182(11):1419–1425.
10. Nureki SI, et al. Expression of mutant Sftpc in murine alveolar epithelia drives spontaneous lung fibrosis. *J Clin Invest*. 2018;128(9):4008–4024.
11. Wert SE, Whitsett JA, Nogee LM. Genetic disorders of surfactant dysfunction. *Pediatr Dev Pathol*. 2009;12(4):253–274.
12. Kabore AF, Wang WJ, Russo SJ, Beers MF. Biosynthesis of surfactant protein C: characterization of aggresome formation by EGFP chimeras containing propeptide mutants lacking conserved cysteine residues. *J Cell Sci*. 2001;114(Pt 2):293–302.
13. Maguire JA, Mulugeta S, Beers MF. Endoplasmic reticulum stress induced by surfactant protein C BRICHOS mutants promotes proinflammatory signaling by epithelial cells. *Am J Respir Cell Mol Biol*. 2011;44(3):404–414.
14. Maguire JA, Mulugeta S, Beers MF. Multiple ways to die: delineation of the unfolded protein response and apoptosis induced by surfactant protein C BRICHOS mutants. *Int J Biochem Cell Biol*. 2012;44(1):101–112.
15. Mulugeta S, Nguyen V, Russo SJ, Muniswamy M, Beers MF. A surfactant protein C precursor protein BRICHOS domain mutation causes endoplasmic reticulum stress, proteasome dysfunction, and caspase 3 activation. *Am J Respir Cell Mol Biol*. 2005;32(6):521–530.
16. Wang WJ, Mulugeta S, Russo SJ, Beers MF. Deletion of exon 4 from human surfactant protein C results in aggresome forma-

tion and generation of a dominant negative. *J Cell Sci*. 2003;116(Pt 4):683–692.
17. Lawson WE, et al. Endoplasmic reticulum stress in alveolar epithelial cells is prominent in IPF: association with altered surfactant protein processing and herpesvirus infection. *Am J Physiol Lung Cell Mol Physiol*. 2008;294(6):L1119–L1126.
18. Bridges JP, Wert SE, Nogee LM, Weaver TE. Expression of a human surfactant protein C mutation associated with interstitial lung disease disrupts lung development in transgenic mice. *J Biol Chem*. 2003;278(52):52739–52746.
19. Lawson WE, et al. Endoplasmic reticulum stress enhances fibrotic remodeling in the lungs. *Proc Natl Acad Sci USA*. 2011;108(26):10562–10567.
20. Willander H, et al. High-resolution structure of a BRICHOS domain and its implications for anti-amyloid chaperone activity on lung surfactant protein C. *Proc Natl Acad Sci USA*. 2012;109(7):2325–2329.
21. Hepping N, Griese M, Lohse P, Garbe W, Lange L. Successful treatment of neonatal respiratory failure caused by a novel surfactant protein C p.Cys121Gly mutation with hydroxychloroquine. *J Perinatol*. 2013;33(6):492–494.
22. Fritsch A, et al. A hypomorphic mouse model of dystrophic epidermolysis bullosa reveals mechanisms of disease and response to fibroblast therapy. *J Clin Invest*. 2008;118(5):1669–1679.
23. Carmeliet P, et al. Abnormal blood vessel development and lethality in embryos lacking a single VEGF allele. *Nature*. 1996;380(6573):435–439.
24. Glasser SW, et al. Altered stability of pulmonary surfactant in SP-C-deficient mice. *Proc Natl Acad Sci USA*. 2001;98(11):6366–6371.
25. Schwenk F, Baron U, Rajewsky K. A cre-transgenic mouse strain for the ubiquitous deletion of loxP-flanked gene segments including deletion in germ cells. *Nucleic Acids Res*. 1995;23(24):5080–5081.
26. Thouvenin G, et al. Characteristics of disorders associated with genetic mutations of surfactant protein C. *Arch Dis Child*. 2010;95(6):449–454.
27. Nogee LM, Dunbar AE, Wert SE, Askin F, Hamvas A, Whitsett JA. A mutation in the surfactant protein C gene associated with familial interstitial lung disease. *N Engl J Med*. 2001;344(8):573–579.
28. Hamvas A, et al. Progressive lung disease and surfactant dysfunction with a deletion in surfactant protein C gene. *Am J Respir Cell Mol Biol*. 2004;30(6):771–776.
29. Wang WJ, Russo SJ, Mulugeta S, Beers MF. Biosynthesis of surfactant protein C (SP-C). Sorting of SP-C proprotein involves homomeric association via a signal anchor domain. *J Biol Chem*. 2002;277(22):19929–19937.
30. Johansson H, Nordling K, Weaver TE, Johansson J. The Brichos domain-containing C-terminal part of pro-surfactant protein C binds to an unfolded poly-val transmembrane segment. *J Biol Chem*. 2006;281(30):21032–21039.
31. Brasch F, et al. Interstitial lung disease in a baby with a de novo mutation in the SFTPC gene. *Eur Respir J*. 2004;24(1):30–39.
32. Jeannotte L, Aubin J, Bourque S, Lemieux M, Montaron S, Provencher St-Pierre A. Unsuspected effects of a lung-specific Cre deleter mouse line. *Genesis*. 2011;49(3):152–159.
33. Beers MF, Kim CY, Dodia C, Fisher AB. Localization, synthesis, and processing of surfactant protein SP-C in rat lung analyzed by epitope-specific antipeptide antibodies. *J Biol Chem*. 1994;269(32):20318–20328.
34. Mulugeta S, Beers MF. Processing of surfactant protein C requires a type II transmembrane topology directed by juxtamembrane positively charged residues. *J Biol Chem*. 2003;278(48):47979–47986.
35. Johnson AL, et al. Post-translational processing of surfactant protein-C proprotein: targeting motifs in the NH(2)-terminal flanking domain are cleaved in late compartments. *Am J Respir Cell Mol Biol*. 2001;24(3):253–263.
36. Beers MF, et al. A nonaggregating surfactant protein C mutant is misdirected to early endosomes and disrupts phospholipid recycling. *Traffic*. 2011;12(9):1196–1210.
37. Barbas-Filho JV, Ferreira MA, Sesso A, Kairalla RA, Carvalho CR, Capelozzi VL. Evidence of type II pneumocyte apoptosis in the pathogenesis of idiopathic pulmonary fibrosis (IFP)/usual interstitial pneumonia (UIP). *J Clin Pathol*. 2001;54(2):132–138.
38. Plataki M, Koutsopoulos AV, Darivianaki K, Delides G, Siafakas NM, Bouros D. Expression of apoptotic and antiapoptotic markers in epithelial cells in idiopathic pulmonary fibrosis. *Chest*. 2005;127(1):266–274.
39. Misharin AV, et al. Monocyte-derived alveolar macrophages drive lung fibrosis and persist in the lung over the life span. *J Exp Med*. 2017;214(8):2387–2404.
40. Gibbons MA, et al. Ly6Chi monocytes direct alternatively activated profibrotic macrophage regulation of lung fibrosis. *Am J Respir Crit Care Med*. 2011;184(5):569–581.
41. Papiris SA, et al. High levels of IL-6 and IL-8 characterize early-on idiopathic pulmonary fibrosis acute exacerbations. *Cytokine*. 2018;102:168–172.
42. Tomos I, et al. IL-6 and IL-8 in stable and exacerbated IPF patients and their association to outcome. *Eur Respir J*. 2016;48(suppl 60): PA3890.
43. Zepp JA, et al. Distinct mesenchymal lineages and niches promote epithelial self-renewal and myofibrogenesis in the lung. *Cell*. 2017;170(6):1134–1148.e10.
44. Belperio JA, et al. The role of the Th2 CC chemokine ligand CCL17 in pulmonary fibrosis. *J Immunol*. 2004;173(7):4692–4698.
45. Yogo Y, et al. Macrophage derived chemokine (CCL22), thymus and activation-regulated chemokine (CCL17), and CCR4 in idiopathic pulmonary fibrosis. *Respir Res*. 2009;10:80.
46. Neighbors M, et al. Prognostic and predictive biomarkers for patients with idiopathic pulmonary fibrosis treated with pirfenidone: post-hoc assessment of the CAPACITY and ASCEND trials. *Lancet Respir Med*. 2018;6(8):615–626.
47. Choi ES, et al. Enhanced monocyte chemoattractant protein-3/CC chemokine ligand-7 in usual interstitial pneumonia. *Am J Respir Crit Care Med*. 2004;170(5):508–515.
48. Car BD, Meloni F, Luisetti M, Semenzato G, Gialdroni-Grassi G, Walz A. Elevated IL-8 and MCP-1 in the bronchoalveolar lavage fluid of patients with idiopathic pulmonary fibrosis and pulmonary sarcoidosis. *Am J Respir Crit Care Med*. 1994;149(3 Pt 1):655–659.
49. Suga M, Iyonaga K, Ichiyasu H, Saita N, Yamasaki H, Ando M. Clinical significance of MCP-1 levels in BALF and serum in patients with interstitial lung diseases. *Eur Respir J*. 1999;14(2):376–382.
50. Rosas IO, et al. MMP1 and MMP7 as potential peripheral blood biomarkers in idiopathic pulmonary fibrosis. *PLoS Med*. 2008;5(4):e93.
51. Tanjore H, Lawson WE, Blackwell TS. Endoplasmic reticulum stress as a pro-fibrotic stimulus. *Biochim Biophys Acta*.

2013;1832(7):940–947.
52. Burman A, Tanjore H, Blackwell TS. Endoplasmic reticulum stress in pulmonary fibrosis. *Matrix Biol*. 2018;68-69:355–365.
53. Tang YW, et al. Herpesvirus DNA is consistently detected in lungs of patients with idiopathic pulmonary fibrosis. *J Clin Microbiol*. 2003;41(6):2633–2640.
54. Stewart JP, et al. The detection of Epstein-Barr virus DNA in lung tissue from patients with idiopathic pulmonary fibrosis. *Am J Respir Crit Care Med*. 1999;159(4 Pt 1):1336–1341.
55. Thannickal VJ. Mechanistic links between aging and lung fibrosis. *Biogerontology*. 2013;14(6):609–615.
56. Collard HR. The age of idiopathic pulmonary fibrosis. *Am J Respir Crit Care Med*. 2010;181(8):771–772.
57. Torres-González E, et al. Role of endoplasmic reticulum stress in age-related susceptibility to lung fibrosis. *Am J Respir Cell Mol Biol*. 2012;46(6):748–756.
58. Balch WE, et al. Malfolded protein structure and proteostasis in lung diseases. *Am J Respir Crit Care Med*. 2014;189(1):96–103.
59. Mulugeta S, Maguire JA, Newitt JL, Russo SJ, Kotorashvili A, Beers MF. Misfolded BRICHOS SP-C mutant proteins induce apoptosis via caspase-4- and cytochrome c-related mechanisms. *Am J Physiol Lung Cell Mol Physiol*. 2007;293(3):L720–L729.
60. White ES, et al. Plasma surfactant protein-D, matrix metalloproteinase-7, and osteopontin index distinguishes idiopathic pulmonary fibrosis from other idiopathic interstitial pneumonias. *Am J Respir Crit Care Med*. 2016;194(10):1242–1251.
61. Konishi K, et al. Gene expression profiles of acute exacerbations of idiopathic pulmonary fibrosis. *Am J Respir Crit Care Med*. 2009;180(2):167–175.
62. Pesci A, Ricchiuti E, Ruggiero R, De Micheli A. Bronchoalveolar lavage in idiopathic pulmonary fibrosis: what does it tell us? *Respir Med*. 2010;104 Suppl 1:S70–S73.
63. Miani M, Colli ML, Ladrière L, Cnop M, Eizirik DL. Mild endoplasmic reticulum stress augments the proinflammatory effect of IL-1β in pancreatic rat β-cells via the IRE1α/XBP1s pathway. *Endocrinology*. 2012;153(7):3017–3028.
64. Hu P, Han Z, Couvillon AD, Kaufman RJ, Exton JH. Autocrine tumor necrosis factor alpha links endoplasmic reticulum stress to the membrane death receptor pathway through IRE1alpha-mediated NF-kappaB activation and down-regulation of TRAF2 expression. *Mol Cell Biol*. 2006;26(8):3071–3084.
65. Dela Peña A, Leclercq I, Field J, George J, Jones B, Farrell G. NF-kappaB activation, rather than TNF, mediates hepatic inflammation in a murine dietary model of steatohepatitis. *Gastroenterology*. 2005;129(5):1663–1674.
66. Gargalovic PS, et al. The unfolded protein response is an important regulator of inflammatory genes in endothelial cells. *Arterioscler Thromb Vasc Biol*. 2006;26(11):2490–2496.
67. McCubbrey AL, et al. Deletion of c-FLIP from CD11bhi macrophages prevents development of bleomycin-induced lung fibrosis. *Am J Respir Cell Mol Biol*. 2018;58(1):66–78.
68. Young LR, et al. Epithelial-macrophage interactions determine pulmonary fibrosis susceptibility in Hermansky-Pudlak syndrome. *JCI Insight*. 2016;1(17):e88947.
69. Atochina-Vasserman EN, et al. Early alveolar epithelial dysfunction promotes lung inflammation in a mouse model of Hermansky-Pudlak syndrome. *Am J Respir Crit Care Med*. 2011;184(4):449–458.
70. Saito A, et al. Modeling pulmonary alveolar microlithiasis by epithelial deletion of the Npt2b sodium phosphate cotransporter reveals putative biomarkers and strategies for treatment. *Sci Transl Med*. 2015;7(313):313ra181.
71. Raghu G, et al. CC-chemokine ligand 2 inhibition in idiopathic pulmonary fibrosis: a phase 2 trial of carlumab. *Eur Respir J*. 2015;46(6):1740–1750.
72. Sisson TH, et al. Targeted injury of type II alveolar epithelial cells induces pulmonary fibrosis. *Am J Respir Crit Care Med*. 2010;181(3):254–263.
73. Garcia O, et al. Targeted type 2 alveolar cell depletion. a dynamic functional model for lung injury repair. *Am J Respir Cell Mol Biol*. 2016;54(3):319–330.
74. Barkauskas CE, et al. Type 2 alveolar cells are stem cells in adult lung. *J Clin Invest*. 2013;123(7):3025–3036.
75. Roberson EC, et al. Influenza induces endoplasmic reticulum stress, caspase-12-dependent apoptosis, and c-Jun N-terminal kinase-mediated transforming growth factor-β release in lung epithelial cells. *Am J Respir Cell Mol Biol*. 2012;46(5):573–581.
76. Tamaki N, et al. CHOP deficiency attenuates cholestasis-induced liver fibrosis by reduction of hepatocyte injury. *Am J Physiol Gastrointest Liver Physiol*. 2008;294(2):G498–G505.
77. Zhang M, et al. Chop deficiency prevents UUO-induced renal fibrosis by attenuating fibrotic signals originated from Hmgb1/TLR4/NFκB/IL-1β signaling. *Cell Death Dis*. 2015;6:e1847.
78. Henderson NC, et al. Targeting of αv integrin identifies a core molecular pathway that regulates fibrosis in several organs. *Nat Med*. 2013;19(12):1617–1624.
79. Jain D, et al. SP-D-deficient mice are resistant to hyperoxia. *Am J Physiol Lung Cell Mol Physiol*. 2007;292(4):L861–L871.
80. Beers MF, Lomax C. Synthesis and processing of hydrophobic surfactant protein C by isolated rat type II cells. *Am J Physiol*. 1995;269(6 Pt 1):L744–L753.
81. Beers MF, Bates SR, Fisher AB. Differential extraction for the rapid purification of bovine surfactant protein B. *Am J Physiol*. 1992;262(6 pt 1):L773–L778.
82. Misharin AV, Morales-Nebreda L, Mutlu GM, Budinger GR, Perlman H. Flow cytometric analysis of macrophages and dendritic cell subsets in the mouse lung. *Am J Respir Cell Mol Biol*. 2013;49(4):503–510.
83. Burns JL, et al. Microbiology of sputum from patients at cystic fibrosis centers in the United States. *Clin Infect Dis*. 1998;27(1):158–163.
84. Gold L, et al. Aptamer-based multiplexed proteomic technology for biomarker discovery. *PLoS One*. 2010;5(12):e15004.
85. Kim CH, et al. Stability and reproducibility of proteomic profiles measured with an aptamer-based platform. *Sci Rep*. 2018;8(1):8382.